UNIVERSITY OF OKLAHOMA

GRADUATE COLLEGE

SEISMICITY AND SOURCE SPECTRA ANALYSIS IN SALTON SEA GEOTHERMAL FIELD

A THESIS

SUBMITTED TO THE GRADUATE FACULTY

in partial fulfillment of the requirements for the

Degree of

MASTER OF SCIENCE

By

YIFANG CHENG
Norman, Oklahoma
2016

SEISMICITY AND SOURCE SPECTRA ANALYSIS IN SALTON SEA GEOTHERMAL FIELD

A THESIS APPROVED FOR THE
CONOCOPHILLIPS SCHOOL OF GEOLOGY AND GEOPHYSICS

BY

_____
Dr. Xiaowei Chen, Chair

_____
Dr. Kurt Marfurt

_____
Dr. Ze'ev Reches

Acknowledgements

I would like to humbly thank Dr. Xiaowei Chen for giving me the opportunity to pursue my graduate studies and thesis research in geophysics, for her guidance in my research and my daily life. Dr. Xiaowei Chen has been patient with me and provided me with scope to think and figure out what I wished to do. She also provide me with many opportunities to attend conferences, which not only help me to comprehensively understand my project, but also inspire me to pursue a PhD degree in geophysics.

I would also like to extend my thanks and gratitude to my committee members, Dr. Kurt Marfurt for his geophysical insight, advice, and encouragement. His passion to exploration geophysics and his AASPI software inspires me to work hard on my research and establish software for my own research.

I would like to acknowledge Dr. Ze'ev Reches for his geological insight and guidance. His ambition and persistence to research motivated and excited me to think about unsolved problem and find out what I want to study.

I would like to express my sincere thanks to Dr. Chastity Aiken for helping me to improve my manuscript. She shared a lot of her PhD experiences to me and encourages me to pursue a PhD degree.

Last but not the least, I would like to thank my family and my friends for their encouragement throughout the pursuit of my Master's degree.

Table of Contents

List of Tables

List of Figures

Abstract

The surge of "man-made" earthquakes in recent years has led to considerable concerns about the associated hazards. Improved monitoring of small earthquakes would significantly help understand such phenomena and the underlying physical mechanisms. In the Salton Sea Geothermal field in southern California, open access of a local borehole network provides a unique opportunity to better understand the seismicity characteristics, the related earthquake hazards, and the relationship with the geothermal system, tectonic faulting and other physical conditions. We obtain high-resolution earthquake locations in the Salton Sea Geothermal Field, analyze characteristics of spatiotemporal isolated earthquake clusters, magnitude-frequency distributions and spatial variation of stress drops. The analysis reveals spatial coherent distributions of different types of clustering, *b*-value distributions, and stress drop distribution. The mixture type clusters (short-duration rapid bursts with high aftershock productivity) are predominately located within active geothermal field that correlate with high *b*-value, low stress drop microearthquake clouds, while regular aftershock sequences and swarms are distributed throughout the study area. The differences between earthquakes inside and outside of geothermal operation field suggest a possible way to distinguish directly induced seismicity due to energy operation versus typical seismic slip driven sequences. The spatial coherent *b*-value distribution enables in-situ estimation of probabilities for M≥3 earthquakes, and shows that the high large-magnitude-event (LME) probability zones with high stress drop are likely associated with tectonic faulting. The high stress drop in shallow (1-3 km) depth indicates the existence of active faults, while low stress drops near injection wells likely corresponds

to the seismic response to fluid injection. I interpret the spatial variation of seismicity and source characteristics as the result of fluid circulation, the fracture network, and tectonic faulting.

Chapter 1. Introduction

Geothermal energy is an important source of renewable, clean energy. The geothermal reservoir is generally defined as the region with over 200 ℃/km thermal gradient in the 30-80 m depth [*Hulen et al.*, 2002]. To access these reservoirs, wells are drilled to as far as 2 km depth. Geothermal technology uses thermal energy by pumping cold water into the reservior, and extracting hot water out of the reservoir to generate electricity.

Geothermal production is usually associated with induced seismicity [e.g., *Schoenball et al.*, 2015; *Trugman et al.*, 2016; *Zaliapin & Ben-Zion*, 2016] – a phenomenon that receives increased level of public concerns due to the increased seismicity rate and the associated seismic hazard in the recent years [e.g., *Ellsworth et al.*, 2013]. Fluid injection and extraction can induce earthquake by the alternation of the pore pressure, regional subsurface stresses, chemical or thermal properties [*Ellsworth et al.*, 2013]. To make a balance between the benefits of geothermal efficiency and the drawbacks, distinguishing low and relatively higher risk activities is needed before and during geothermal operation. In my thesis, I analyze the earthquake data in Salton Sea Geothermal Field (SSGF) to identify the risk factors and quantify the hazard, which is helpful to the decisions in geothermal production.

Similar to earthquakes of tectonic or volcanic origin, induced earthquakes occur when stresses on pre-existing planes of weakness exceed their strength [*Scholz*, 1990]. However, the difference is that the stress or strength changes are perturbed by anthropogenic influences for induced seismicity [*Trifu*, 2002]. The actual underlying physical mechanism of rupture process due to injection of fluid is not yet fully understood. Moreover, seismic response to fluid injection changes depending on the

variation of rock properties, injection pressure, fluid volume and temperature. The total number of induced events is in general proportional to injected fluid volume in spite of regional differences [*Shapiro et al.*, 2007; *McGarr*, 1976]. Many of the large-magnitude event (LME) reported have occurred after long-term fluid injection [*Frohlich et al.*, 2011] and tend to occur on developed or active fault systems [*Evans*, 2005]. *Shapiro et al.* [2010] find significantly higher seismogenic indices for geothermal stimulation in crystalline rocks than for comparable operations in sedimentary formations. Some studies show that induces earthquakes have lower stress drop at areas with higher pore pressure [e.g., *Goertz-Allmann et al.*, 2011], and may have lower stress drop compared to tectonic earthquakes [e.g., *Hough*, 2002]; however, other studies suggest that they have comparable stress drops [e.g., *Tomic et al.*, 2009], and that the main factors influence stress drop are the geology and tectonic settings [e.g., *Shearer et al.*, 2006; *Allmann and Shearer*, 2007; *Abercrombie and Leary*, 1993]. Due to the complex geological setting and spatio-temporal variation of fluid injection, it is often difficult to quantify the seismic response to fluid injected. How do fluid injection and pressure affect event size and frequency? And what is the relationship between geological settings and large magnitude events? Such unknown motivates further research into the statistics and physics of induced earthquakes and the potential for inducing large-magnitude events.

The SSGF lies within one of the most seismically active areas in California, and is one of the largest geothermal fields. The SSGF is located within the extensional step-over between the Imperial and Southern end of the San Andreas Fault (Figure 1) [*Muffler and White*, 1969; *Crowell et al.*, 2013], that experiences significant amount of

subsidence and accommodates partial plate motion between the North America Plate and the Pacific Plate [*Brothers et al.,* 2009]. The SSGF exhibits dramatic variations of temperature and lithology because of the existence of the magmatic intrusion [*Younker et al.*, 1982; *Hulen and Pulka*, 2001]. In addition to the tectonic motion, the field features frequent injection/production activities [*Brodsky and Lajoie, 2013*] (Figure 2), as well as seismic and aseismic slips [*Lohman and McGuire*, 2007; *Catchings et al*., 2010] just across a few kilometers area. Previous study shows that the earthquake in the SSGF had a noticeable change after the beginning of the geothermal operation [*Zaliapin and Ben-Zion*, 2016]. It provides a good opportunity to investigate the effect of environmental conditions on the induced seismicity within a major tectonic zone.

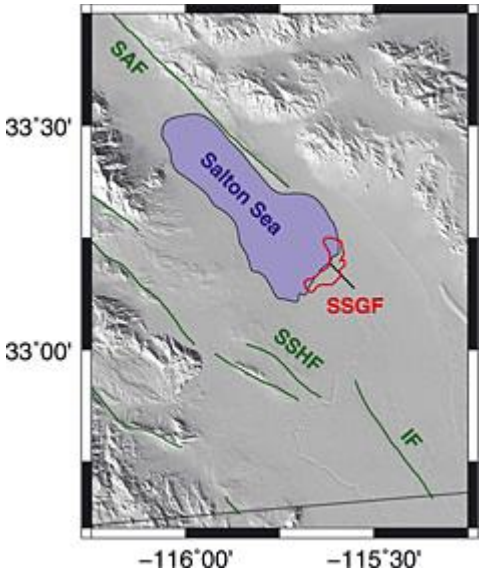

Figure 1. Regional shaded relief map of the Salton Trough area showing the Salton Sea Geothermal Field (SSGF in red) as well as the San Andreas Fault (SAF), Imperial Fault (IF), and Superstition Hills Fault (SSHF) from the Southern California Earthquake Center Community Fault model. Blue shows the location of the Salton Sea (From Figure 1 in *McGuire et al.*, 2015).

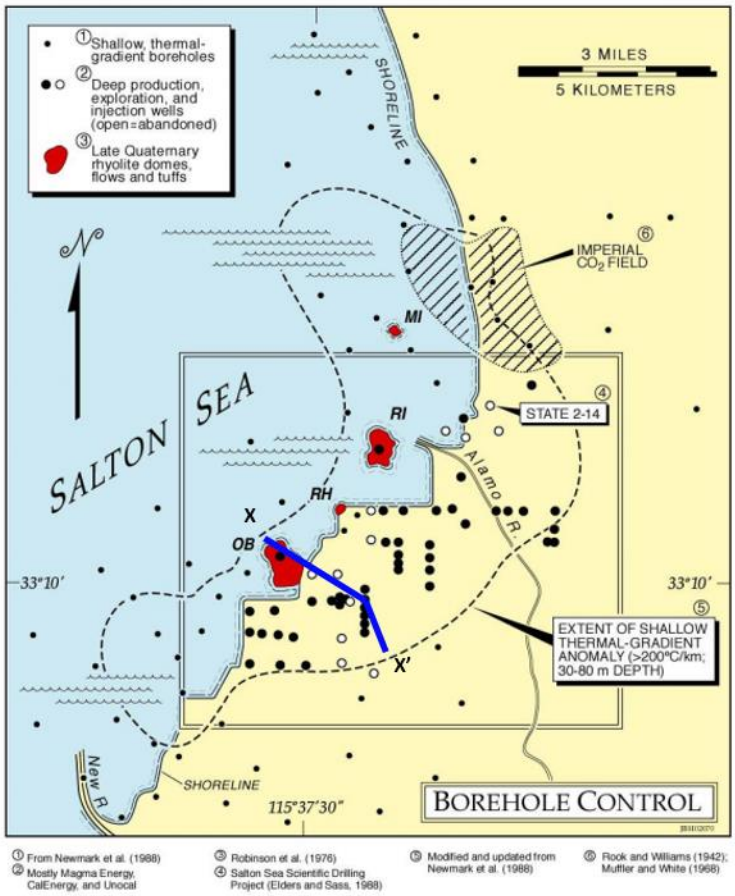

Figure 2. Production wells, injection wells as well as borehole control for an updated shallow thermal-gradient map of the Salton Sea Geothermal Field and vicinity (From *Hulen et al.*, 2002). The blue line denoted the XX' cross section of Hulen et al. [2003] shown in Figure 4.

The study of the induced seismicity in the SSGF also benefit from dense observations of subsurface properties, seismicity and deformation. Numerous geothermal exploration wells and drill cutting and core samples provide information about reservoir geology. The sedimentary sequence in the study area can be separated into three categories (Figure. 3): (1) impermeable cap rock within high heat flow, primarily conductive region (~500 m); (2) upper, slightly altered reservoir rock with high porosity and significant fracturing (1000-2000 m); (3) lower, extensively altered reservoir rock with reduced porosity [*Younker et al.*, 1982; *Clayton et al.*, 1968]. And

many deep wells (Figure 4) penetrate sedimentary rocks containing concentrated brines where temperatures exceeding 320 ℃ at only 2 km depth [*Muffler and White*, 1969]. Therefore, the typical brittle-ductile transition zone which controls the maximum earthquake nucleation depth should occur at shallower depths than the rest of California [*McGuire et al.*, 2015]. And the shallow part of study area also features with tectonic fault system. The major structural feature is the Main Central Fault (MCF) zone (Figure 4) which was interpreted as a left-lateral, strike-slip fault [*McGuire et al.*, 2015]. Between 2008 and 2014, a local borehole network was made available to the public through the SCEC (Southern California Earthquake Center) data center. These high-quality waveforms significantly improve the monitoring of small earthquakes, thus provide an unprecedented opportunity to analyze seismicity distribution and source mechanism in great details.

Unit	Lithology	Heat transfer
Cap rock	Thick unconsolidated silt, sand, gravel, and anhydrite-rich deposits	Heat flow by conduction
Slightly altered reservoir	Shale and sand Small sand units	Enhanced conductivity resulting from presence of sand; still part of thermal cap
	Upper reservoir Shales, siltstone, and sandstone cemented by calcite or silica	Convection within sand units; shales separate region into isolated hydrologic systems
	Major shale break	
Highly altered reservoir	Lower reservoir Reduced permeability results when altered by replacement of calcite with epidote; extensively fractured	Fractures allow more extensive convection patterns
Zone of intrusion	Intrusion of small basaltic dikes and sills into sedimentary section; less than 20% intrusive bodies	Rate of heat release is a function of rate of intrusion

Figure 3. After Figure 20 of *Younker et al.* [1982]. The relationship between the lithology and the heat transfer characteristics at different zones from cap rock down to zone of intrusion.

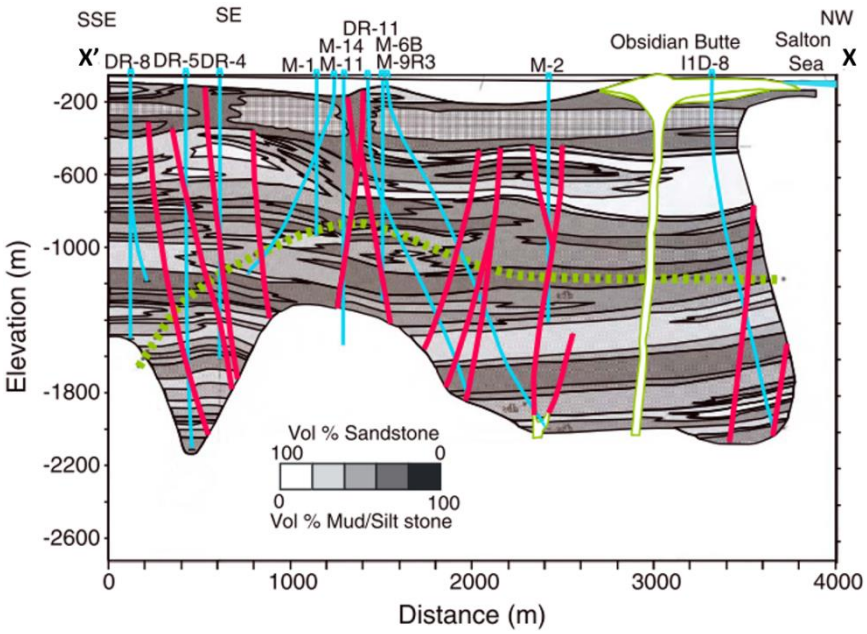

Figure 4. After Figure 5 of *Hulen et al.* [2003]. Geological cross section along the X to X' line shown in Figure 2. Gray scale colors represent lithology ranging from 100% (white) to 0% (black) sandstone (see *Hulen et al.* [2003] for details). Individual geothermal wells are shown in light blue and labeled along the top. Major faults interpreted by *Hulen et al.* [2003] are shown in red. The dashed green line denotes the upper limit of the geothermal reservoir (roughly 275°C). The Main Central Fault consists of multiple strands that intersect the surface near wells DR-11 and M-6B. From Figure 3 of *McGuire et al.* [2015].

My thesis focuses on the analysis of seismicity characteristics, source parameters associated with fluid injection, intrusion, and aseismic creep in the Salton Sea Geothermal Field. The analysis utilizes 2008-2014 seismic data from a local borehole network, with two main objectives: (1) to map the spatial distribution of b-value, cluster types and seismicity rate in relation to fluid injection; and (2) to analyze the source spectra to estimate the stress drop distribution. For the first objective, I will use the neighboring distance [*Zaliapin and Ben-Zion*, 2013] and single-link method [*Frohlich et al.*, 1990] to identify cluster type and use the maximum likelihood method [*Utsu*, 1965; *Aki*, 1965] to estimate *b*-value distribution. For the second objective, I will

use Empirical Green's Function (EGF) for distributed seismicity to map variations in earthquake source spectral properties in the SSGF. I anticipate that the integrated analysis of the *b*-value, cluster distribution and stress drop spatial distributions will reveal earthquakes distribution in relation to injection/production activities, geological context and other environmental conditions.

Chapter 2 is the analysis of seismicity characteristics and their spatial distribution. This chapter includes three sections: cluster analysis, *b*-value analysis, and large magnitude event probability analysis.

Chapter 3 analyzes the stress drops of events in the SSGF and their spatial distribution. This chapter includes two parts: stress drop estimation and analysis using stacking method, and individual-pair analysis for repeating earthquakes.

Chapter 4 concludes the study and reviews the outcomes of Chapter 2 and Chapter 3.

Chapter 2. Seismicity analysis

Previous study

Previous studies suggest that earthquakes in the Salton Sea Geothermal Field can be triggered by various physical mechanisms. Some events are dynamically triggered by distant large events (e.g., the $M7$ Hector Mines earthquake) because of shear failure at relatively low differential stresses [*Hough and Kanamori*, 2002]. The spatiotemporal correlation of ladder-like expansion of injection wells and seismicity [*Chen and Shearer*, 2011] and the temporal correlation between seismicity rate and the net production volume [*Brodsky and Lajoie*, 2013] provide evidence of induced seismicity. In addition, major earthquake swarms with $M5$ events in the Salton Sea Geothermal Field appear to be driven by aseismic fault slip based on geodetic observations [*Lohman and McGuire*, 2007]. The high seismicity rate, and diversity of triggering processes make it a natural earthquake laboratory to understand the relationship between spatiotemporal patterns of seismicity and different driving forces.

Earthquake dataset

I download triggered waveforms archived in the Southern California Earthquake Data Center (SCEDC) using the seismogram transfer program (STP) and organize the waveforms into event-based file system. Because of the missing S-wave picks on the borehole network, an auto-picker algorithm (Jeff McGuire, personal communication) is applied to obtain more complete S-wave arrivals. We then measure more precise differential times using waveform cross-correlation with a sub-sample accuracy of 0.001s between 2 and 10 Hz. The correlation coefficients are measured for each earthquake with the nearest 500 earthquakes, using time windows of -0.3s before and

0.8s after P-wave arrivals, -0.5s before and 1.0s after S-wave arrivals. Only pairs with cross-correlation coefficients > 0.8 are included for relocation. Over 1.5 million absolute and differential arrival times for 7348 earthquakes are included in double-difference relocation using the tomoDD package [*Zhang and Thurber*, 2003], based on the 3D velocity model in *McGuire et al.* [2015]. The relative location uncertainty is estimated to be 51 m in horizontal direction and 41 m in depth using a bootstrap resampling approach. Figure 5 shows that the averaged absolute residual changed from 0.66 s at the first iteration to 0.03 s at the final iteration.

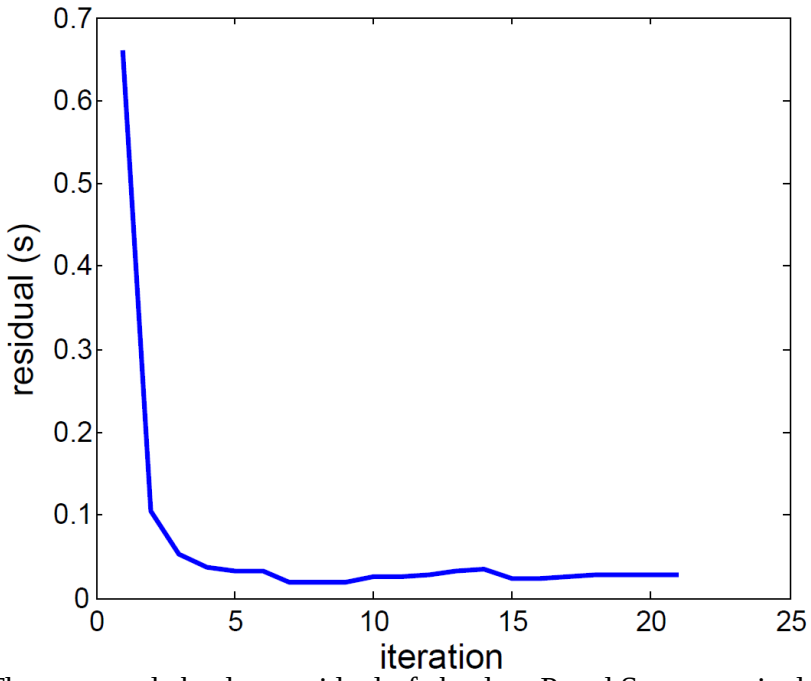

Figure 5. The averaged absolute residual of absolute P and S wave arrival time recorded by 10 stations. The absolute residual changed from 0.66 s at the first iteration to 0.02 s at the last iteration.

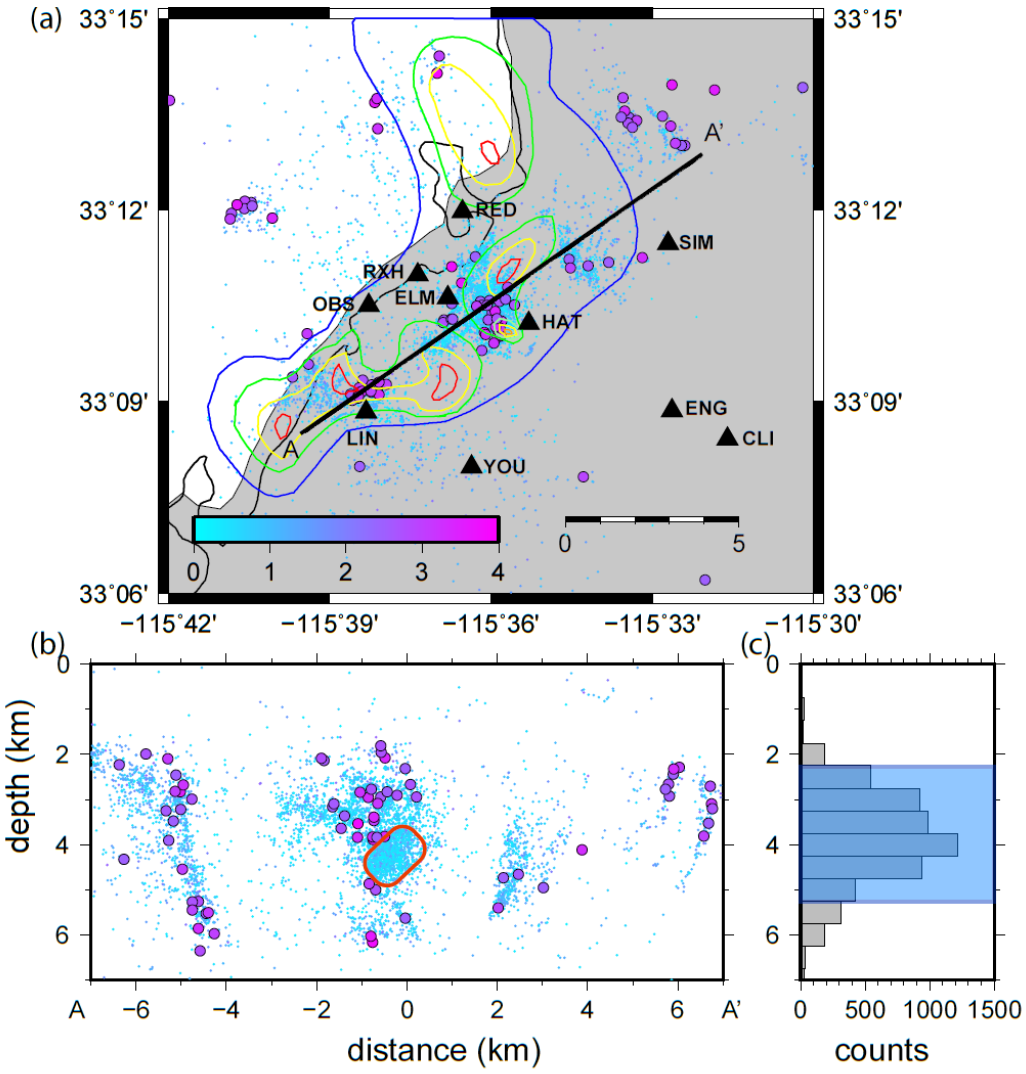

Figure 6. Map (a) and cross-section AA' (b) view of the event and geothermal gradient (colored contour) distribution in Salton Sea Geothermal Field. Stations ELM, HAT, LIN, OBS, RED, SIM, YOU, and ENG are from the CalENergy network; RXH and CLI (small triangle next to ELM, short period vertical only) are from the Southern California Seismic Network. The contours show the $\mathbf{800}$ ℃/**km** (red), $\mathbf{600}$ ℃/**km** (yellow), $\mathbf{400}$ ℃/**km** (green) and $\mathbf{200}$ ℃/**km** (blue) contours of the shallow geothermal gradient from *Hulen et al.* [2002]. The earthquakes are colored by magnitude, with large magnitude ($\boldsymbol{M_L \geq 2.5}$) events plotted circles. Black triangles shows the location of stations. The histogram indicates that most earthquakes are located in between 2km and 5km depth. The red circle area outlines a microseismicity cloud without any events larger than 2.5.

The map in Figure 6a clearly illuminates the three sub-clusters in the geothermal field, which correspond to three groups of injection wells [*Chen and Shearer*, 2011].

The cross-section (AA') view and depth histogram (Figure 6b, 6c) suggest that most events are located between 2 and 5 km. For the middle sub-cluster (with distance between 2km to 1km in Figure 6b), most larger ($M_L > 2.5$) events are located at a shallower depth, and a microearthquake cloud that clearly lacks any larger events occurs between 3 and 5 km depth (outlined red area in Figure 6b).

Wiemer and Wyss [2000] suggested that a careful estimate of the spatial and temporal homogeneity of the magnitude of completeness (M_c) is required to study seismicity characteristics. M_c decreases with time in most earthquake catalogs because of denser networks and methodology developments [*Wiemer and Wyss*, 2000]. I compute a catalog completeness of 0.6 using the maximum curvature method [*Woessner and Wiemer*, 2005], which is significantly lower than Mc = 1.5 before 2008 (Figure 7). In the following analysis except for stress drops analysis, I only use 2471 events with $M_L > 1.0$ (well above the estimated M_c) to ensure the spatiotemporal homogeneity of the catalog.

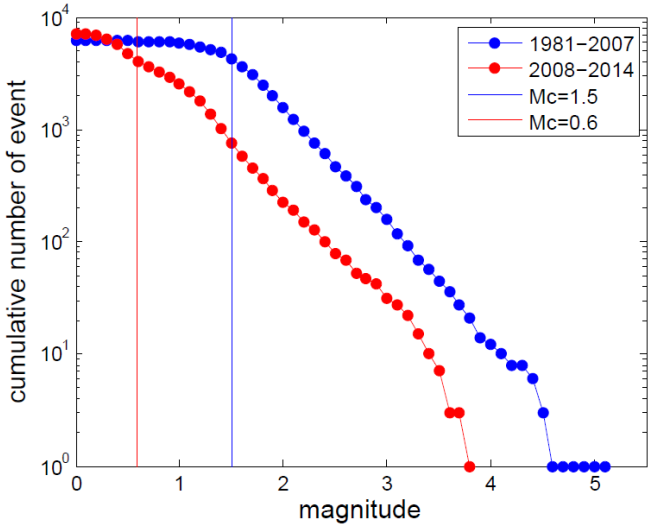

Figure 7. The comparison of magnitude frequency distribution of events in the Salton Sea geothermal field from 1981-2007 (blue) and from 2008-2014 (red). The magnitude

of completeness decreases from 1.5 to 0.6. As a result, we only use events with $\boldsymbol{M_L \geq 1.0}$ (well above the estimated $\boldsymbol{M_c}$) to ensure the spatiotemporal homogeneity of the catalog.

Cluster characteristics

The spatiotemporal clustering of earthquakes is typically divided into aftershocks (with or without foreshocks) and earthquake swarms, which reflect different underlying triggering processes, e.g., earthquake-to-earthquake triggering and aseismic processes [*Mogi*, 1963]. Methods to evaluate temporal clustering of earthquakes include: comparing earthquake sequences to Poisson processes [*Frohlich*, 1987; *Utsu et al.*, 1995; *Kisslinger*, 1996], detecting spatiotemporal clustering (earthquake bursts) with fixed spatiotemporal windows [*Chen and Shearer*, 2011; *Vidale and Shearer*, 2006], single-link cluster analysis [*Frohlich et al.*, 1990] and nearest-neighbor distances [*Zaliapin and Ben-Zion*, 2013]. I set nearest neighbor distance threshold through examination of the spatiotemporal clustering, and then apply a single-link approach [*Frohlich et al.*, 1990] to identify individual clusters. These events are then classified based on parameters related to temporal magnitude distributions.

Cluster identification

For events in the same cluster, they are close to each other both in time and distance. To identify the likelihood of two events in the same cluster, *Zaliapin and Ben-Zion* [2013] computes the near neighbor distance η_{ij} in km$^{1.6}$ between event i and j as

$$\eta_{ij} = \begin{cases} dt_{ij} \times dr_{ij}^{1.6}, & dt_{ij} > 0 \\ \infty, & dt_{ij} \leq 0 \end{cases} \quad (1)$$

where $dt_{ij} = t_j - t_i$ is the inter-event time in days, and dr_{ij} is the inter-event distance in km. For each event j, we find its nearest neighbor, by searching all events that occurred before j ($dt_{ij} > 0$). Event k is called the nearest neighbor to event j with $\eta_{kj} = \min(\eta_{ij})$. Then, we represent the time and space component of the nearest neighbor with:

$$dT_j = dt_{kj}; dR_j = dr_{kj} \quad (2)$$

Figure 8a shows two different modes of nearest neighbors, consistent with observations elsewhere with different threshold $\boldsymbol{\eta}$ values [e.g., *Zaliapin and Ben-Zion*, 2013; *Schoenball et al.*, 2015]. The "clustered" mode has nearest neighbors occurring extremely close in space and time, and the "background" mode represents events that are further separated from their nearest neighbors. Based on Figure 8a, we separate the two groups with $\eta_{thres} = 0.13$. Figure 8a also shows that for clustered events in the SSGF, nearest neighbors tend to occur within 1 day time window following the first event. So I choose $\eta_{thres} = 0.13$ and $dt = 1$ as the empirical thresholds to identify neighbor.

The first step of clustering is to search groups. For each event i in the group, it has all of its neighbor events j in the same group with $dt_{ij} < 1$ and $\eta_{ij} < 0.13$. I search for spatially and temporally isolated groups following the workflow shown in Figure 8c. Each clustered event i in Figure 8a is a potential initial event of a group, and we search for event j with $0<dt_{ij}<1$ day and η_{ij} smaller than 0.13 (where event j occurs after event i) in the catalog. Then, we link target events and their neighbors in the same group. If either target event or its neighbors has already been included in an existing

cluster, then we add other linked events to the same cluster. The process continues until no further events can be linked to the existing clusters. As a result, we identify over 300 groups. However, the majority of the clusters have fewer than 5 events (Figure 8d). Based on the histogram in Figure 8d, we select 49 clusters with more than 7 events (14.37% of total clusters) for further analysis.

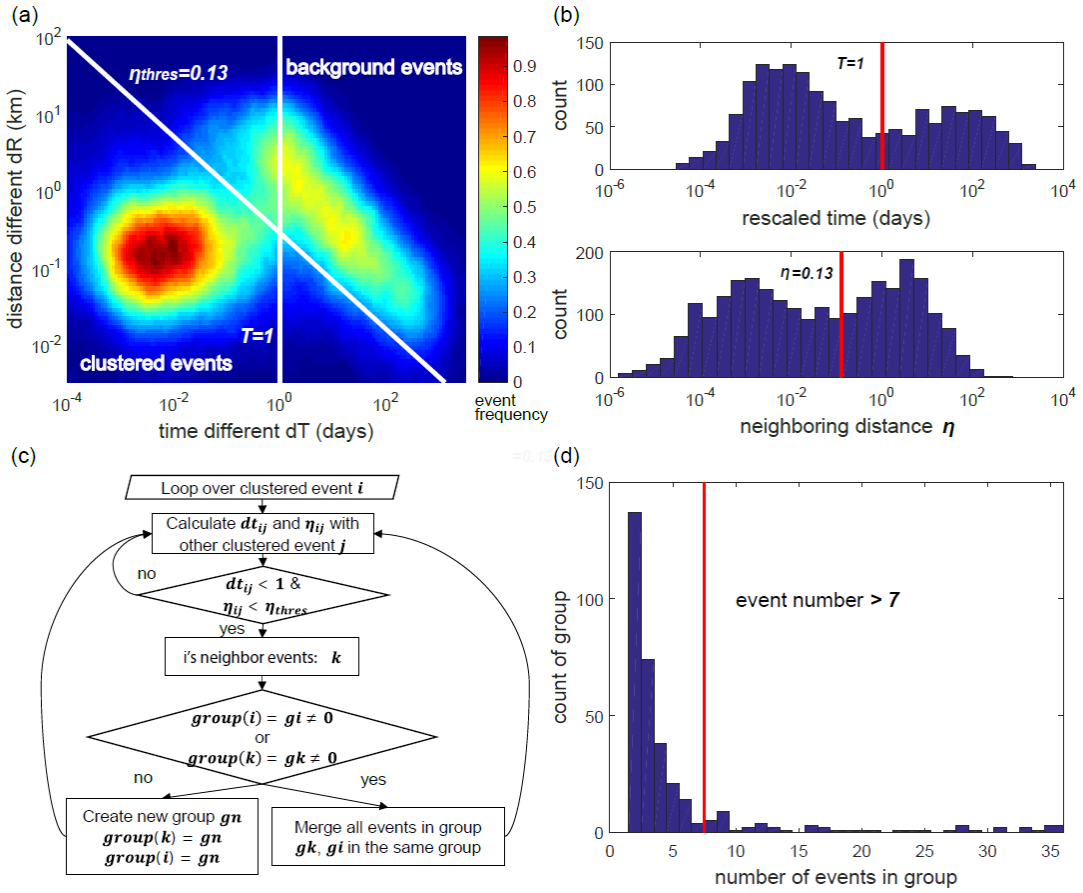

Figure 8. (a) 2D histogram of the nearest-neighbor distance $\boldsymbol{\eta}$ with respect to inter-event distance and time. The vertical white and diagonal lines show the empirical thresholds used to discriminate two events in the same group or not. (b) Histogram of inter-event time and neighboring distance of the nearest neighbor. (c) Workflow for generating groups using single-link method [*Frohlich et al.*, 1990] based on the discriminators shown in (a). (d) Histogram of number of events within each identified cluster. The majority of clusters have fewer than 5 events, and 49 clusters with more than 7 events are selected for subsequent analysis.

Cluster classification

Clusters commonly occur in the form of aftershock sequences and swarms. We attempt to use magnitude-time distribution to separate the swarm-like and aftershock sequences. Aftershock sequences tend to have largest event occurred at the beginning of the cluster, while swarm sequences do not usually start with their largest event. To quantify the temporal magnitude behavior, I compute two parameters: the timing of the largest events t_{max} normalized by the median value (Figure 9), and the skewness value $skew$. For a given cluster, the normalized timing of the largest event t_{max} can be calculated as

$$t_{max} = \frac{t_{main} - t_{first}}{t_{median} - t_{first}}. \quad (3)$$

And for the skewness of moment release, as described in *Roland and McGuire* [2009], pure aftershock sequences (t_{max} = 0) have large positive skew while swarms (larger t_{max}) tend to have lower or even negative skew. For each event, the moment is estimated by the catalog magnitude:

$$M_0(i) = 10^{1.5M_L(i)+9.1}, \quad (4)$$

[*Kanamori*, 1977]. The centroid time of moment release (Figure 9) is obtained using moment weighted mean time:

$$t^* = \frac{\sum_1^N t_i \times M_0(i)}{\sum_1^N M_0(i)}. \quad (5)$$

And individual moment is normalized by

$$m_0(i) = \frac{M_0(i)}{\sum_1^N M_0(i)}. \quad (6)$$

The third central moment of the cluster is $\mu_3 = \sum_1^N (t_i - t^*)^3 m_0(i)$, with standard deviation $\sigma^2 = \sum_1^N (t_i - t^*)^2 m_0(i)$. So the skew of moment release of each cluster is $skew = \mu_3/\sigma^3$.

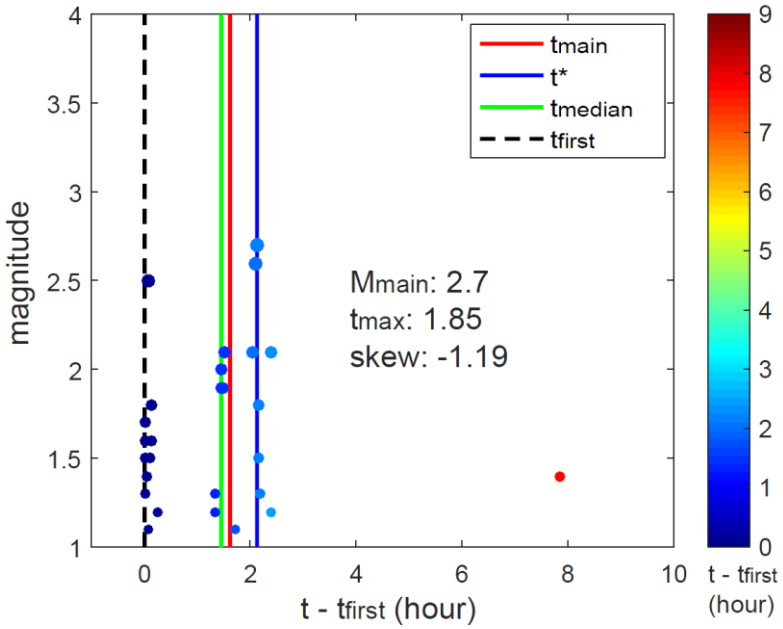

Figure 9. Scatter plot of magnitude and time for representative cluster. The events are colored by time and their sizes are proportional to magnitude. The dashed line shows time of the first event in the cluster, $\boldsymbol{t_{first}}$. The solid lines denotes the median value of events' time in the cluster, $\boldsymbol{t_{median}}$ (green), time of the largest magnitude event, $\boldsymbol{t_{main}}$ (red) and the centroid time $\boldsymbol{t}^*$ (blue).

Figure 10a shows the 2D scatter plot of t_{max} and $skew$ for clusters. Based on different temporal-magnitude behaviors between swarm and aftershock sequences, clusters with large t_{max} have relatively small $skew$, which I classify as swarm-type ($t_{max} \geq 0.5$ and $skew < 6$) (see example in Figure 11b); and clusters with small t_{max} and a relatively larger μ, which I classify as aftershock-type ($t_{max} < 0.5$ and $skew \geq 6$) (see example in Figure 11a). However, some clusters have both small t_{max}, which implies that the largest event occurs early in the sequence (more aftershock

like), and small $skew$, which corresponds to a relatively symmetric moment release history (more swarms like). These are classified as mixture-type ($t_{max} < 0.5$ and $skew < 5$) (see example in Figure 11c). The cut-off values for t_{max} and $skew$ are empirically derived based on the maximum separation between swarm and aftershock-type clusters, and are generally consistent with *Zhang and Shearer* [2016] for the San Jacinto Fault Zone. Overall, out of 49 of clusters, 26 are classified as earthquake swarms, 8 are aftershocks, and 15 are mixture-type.

Cluster characteristics

To further investigate earthquake cluster characteristics, we compute aftershock productivity for each cluster by counting the number of events within each cluster following the largest earthquake (with $M_c = 1$) in 1-day time window. The largest earthquake in each cluster is referred as the "mainshock" in the following text. For comparison, we also include historic large magnitude events ($M_L \geq 4$) using the *Hauksson et al.* [2012] catalog (magenta diamonds in Figure 10b) between 1981 and 2007 in the geothermal field. We require that the selected $M_L \geq 4$ events are sufficiently separated in time (more than 1 year) so as not to interact with each other. For the 1981-2007 earthquake catalog, aftershocks are counted within 1-day time window (with $M_c = 2$). We perform least-square method to find the best fit line to the historic large magnitude events before 2008 (magenta diamonds and line in Figure 10b) to provide a reference of expected number of aftershocks for a given magnitude [*Llenos et al.*, 2009]. Figure 10b shows number of aftershocks versus mainshock magnitude corrected by M_c. For comparison, I also re-examine clusters within the same study area in *Chen and Shearer* [2011]. Under the new criteria in this study, four of clusters are

swarms, and one becomes a mixture (Figure 10b). In *Chen and Shearer* [2011], All clusters are classified as swarms due to the significance of spatial migration depending on time. The result in Figure 10b suggests that for certain magnitude mainshock, mixtures tend to have more aftershocks compared with swarm in 1-day time window.

We further analyze the temporal behavior of different types of clusters. Figure 10c examines the durations (defined as $t_{mean} - t_{first}$) of clusters belonging to different groups. It is noted that the mixture type tend to have much shorter duration compared to swarms and aftershocks. This could be due to the lower mainshock magnitude compared to aftershocks, but we note that the mixture have comparable number of aftershocks to aftershock-type clusters (see Figure 10b), so the shorter duration suggests much concentrated earthquake occurrence, which is further confirmed by the comparison with predicted seismicity rate in Figure 10d. We compute seismicity rate before and after mainshock following a power-law increase and decrease before and after mainshock t_{main}, which is usually termed as inverse Omori's law and Omori's law [*Utsu & Ogata*, 1995, *Hainzl*, 2003]:

In Figure 10d, the temporal seismicity rate increase before mainshock for swarm sequences, and the rate decrease aftershock mainshock for aftershock sequences, are both consistent with the power law prediction; however, the mixture sequence has more concentrated aftershock occurrence rate around the time of the mainshock, and rapid/abrupt temporal decay, consistent with the overall shorter duration for mixture-type clusters.

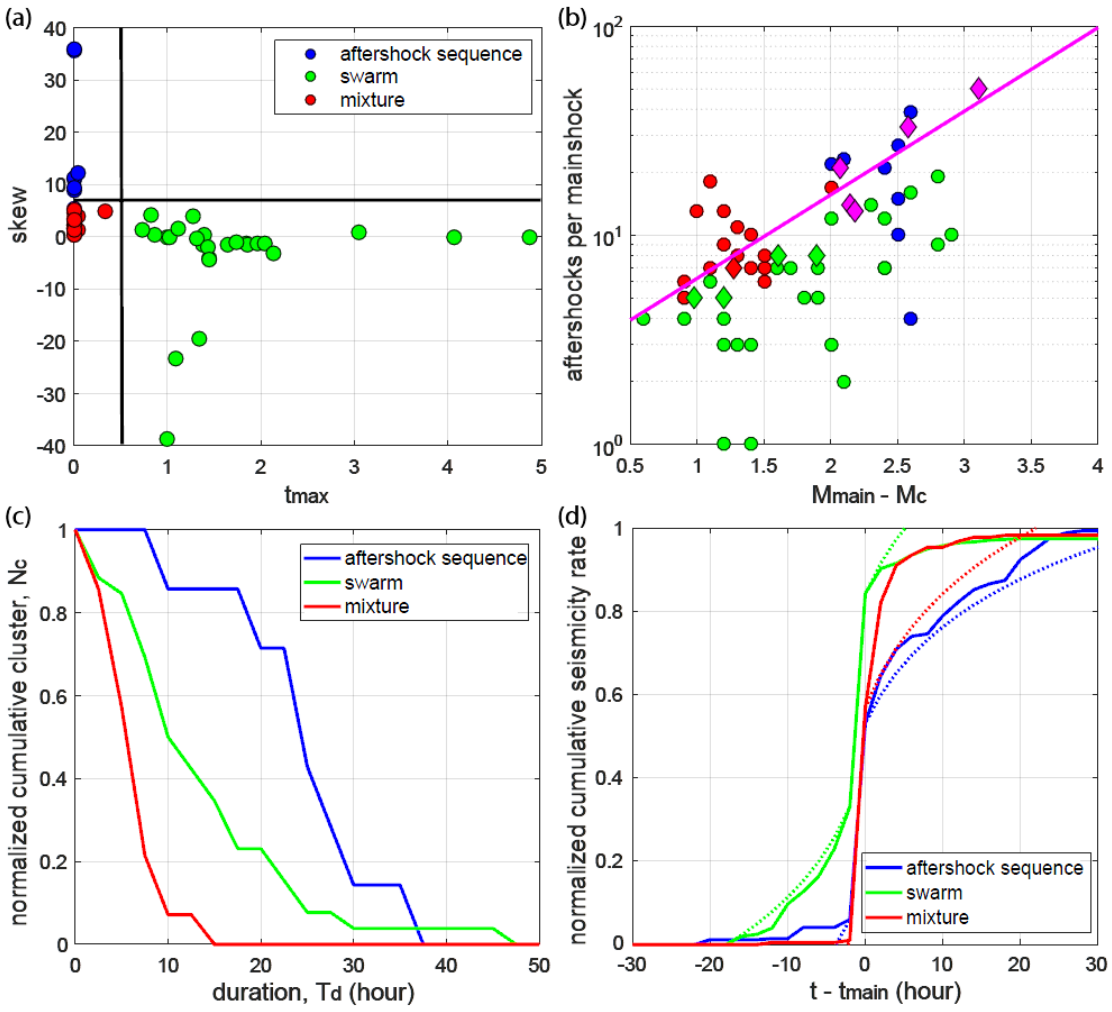

Figure 10. Classification and characteristics for aftershock (blue), swarm (red), and mixture (green) type clusters (see text for more details). (a) Skewness $\boldsymbol{skew}$ versus $\boldsymbol{t_{max}}$ for each cluster. Black lines denote the discriminators used for classification. (b) Number of aftershocks per mainshock in each cluster versus magnitude of mainshock corrected by $\boldsymbol{M_c}$. Clusters from *Chen and Shearer* [2011] are plotted diamonds. The magenta line marks constant aftershock productivity rate per magnitude based on historic large mainshocks ($\boldsymbol{M_L \geq 4}$ since 1981, shown as magenta diamonds). (c) Normalized duration-frequency distribution ($\boldsymbol{F(x) = P(X \geq x)}$) of aftershock sequence (blue), swarm (green) and mixture (red). The normalized number of clusters $\boldsymbol{N_c}$ with duration larger than $\boldsymbol{T_d}$. (d) Stacked cumulative seismicity rate history (relative to the mainshock) for all clusters within each group. The colored dashed lines show the inverse Omori's law and Omori's law curve with decay rate 1.

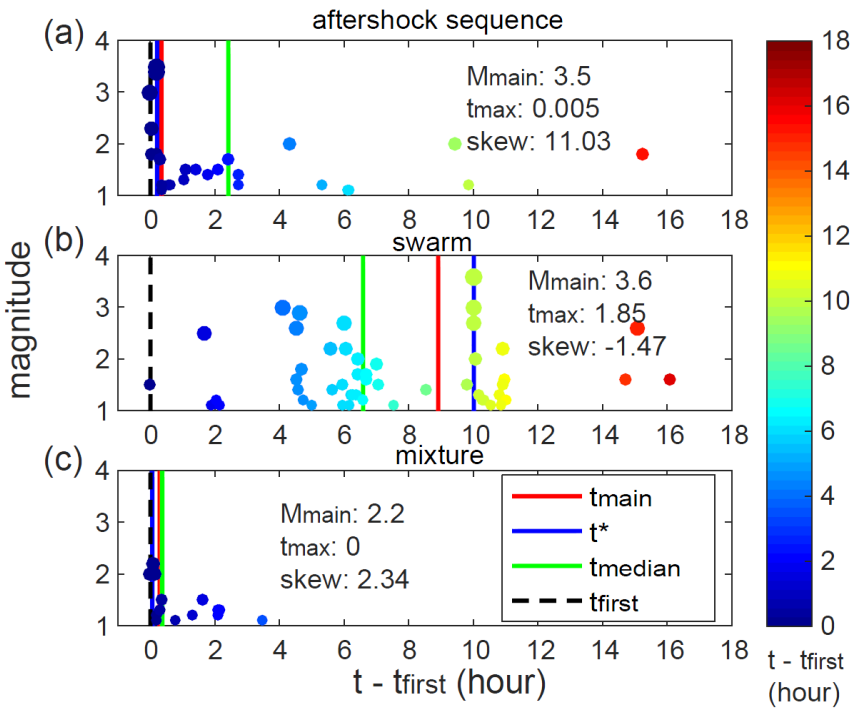

Figure 11. Scatter plot of magnitude and time for representative cluster belonging to aftershock sequence, swarm and mixture. The events are colored by time and their sizes are proportional to magnitude. The dashed line shows time of the first event in the cluster, $\boldsymbol{t_{first}}$. The solid lines denotes the median value of events' time in the cluster, $\boldsymbol{t_{median}}$ (green), time of the largest magnitude event, $\boldsymbol{t_{main}}$ (red) and the centroid time $\boldsymbol{t}^*$ (blue).

Cluster distribution and discussion

To summarize, the mixture-type clusters appear different from both earthquake swarms and aftershocks in terms of temporal decay, aftershock productivity, and duration. For earthquake swarms and aftershock sequences, most of their durations are more than ten hours (Figure 10c); moreover, both the pre-mainshock increase and post-mainshock decrease of aftershock sequences follow Omori's law (Figure 10d). *Chen and Shearer* [2011] also found similar power-law increase/decrease for clusters in the SSGF. The temporal behavior of swarms and aftershock sequences is also consistent

with simulated swarm activities in described by *Hainzl*, [2003] on self-organized seismicity using a spring-block model.

In terms of spatial distributions of different types of clusters, the mixtures are only located within the active geothermal field (Figure 12a). There also appears to be clear depth separation between mixture-type and swarm clusters, at least in the middle of the field (black circle in Figure 12b). The clusters within the geothermal field do not appear to align along a plane as clusters do outside the geothermal field. Based on the spatial pattern of clusters, I attribute the special properties of mixture to the following reasons.

The observations suggest that the mixture-type clustering may represent earthquakes directly induced by the geothermal operation.

1) Unlike aftershock sequence and swarm, most of mixtures have a very short duration (less than 10 hours) (Figure 10d, 11a and c). The more "burst-like" feature suggests that they may be related to short term stress perturbation. The spatial distribution shows that most mixtures are close to injection and production wells, which indicates that the rapid stress change is likely related to the frequent fluid injection activities, which perturb the localized stress field [*Ellsworth et al.*, 2013].
2) Compared with swarms and aftershock sequences, mixtures have small magnitude mainshocks (i.e., $M_{main} \leq 2.5$, see Figure 10b). So mixture is not likely to occur along main tectonic active faults with high strain accumulation. And compared with Omori's law, mixture has much more aftershocks within 3 hours of mainshock ($t - t_{main} < 3$ hour), while few

aftershocks later (Figure 10d). If Omori's law represents typical aftershock decay pattern for faults with a step-like stress change, and relatively constant background stress loading [i.e., *Dieterich* 1994], then the mixture may be resulted from rapid increase of stress loading in the first several hours and rapid decrease of stress loading. So the mixture is most likely caused by the rapid fluid injection on the timescale of a few hours.

3) In contrast to their short duration, mixtures have higher aftershock productivity compared with swarm and aftershock. The higher aftershock productivity is consistent with observations reported by *Llenos and Michael* [2013] for potentially fluid-induced earthquakes in Oklahoma and Arkansas. The higher aftershock productivity of mixture may be related to a weakened highly fractured zone, which repeatedly fails with fast fluid pressure recharge.

It is tempting to compare the timing of mixture-types to injection/production records. However, we note that the time scale for clusters is less than 1 day, while injection pressure and volumes are only reported monthly. The clear differences in temporal resolution limit our capability of direct comparison.

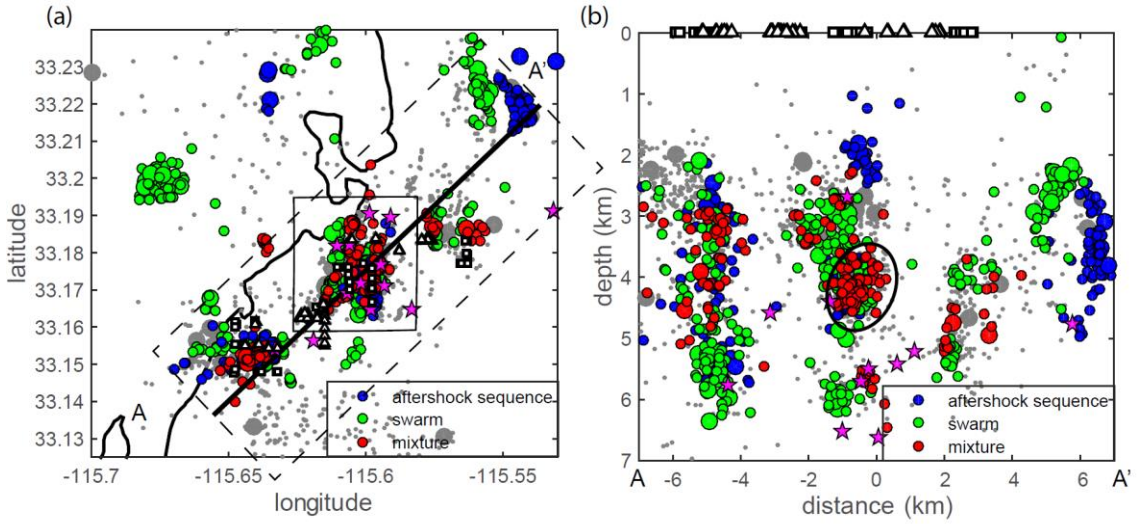

Figure 12. (a) Map view of events and (b) cross-section (AA') view of events in dashed line box colored by cluster type: background events (gray dot) and events belonging to aftershock (blue), swarm (green), and mixture (red) clusters. White square indicates injection well, white triangle is production well and magenta star shows historic large magnitude events with $\boldsymbol{M \geq 4}$ since 1981. Events with $\boldsymbol{M \geq 2.5}$ in our study period are indicated by larger circle. The solid line box is the chosen area for detailed discussion and the black contour shows the boundary of Salton Sea.

Magnitude frequency distribution

Gutenberg-Richter law (GR law) describes the relationship between the magnitude M and the cumulative number of earthquakes N above M_L, in a given volume, which can be written as $log\ N\ (m\ \geq\ M_L))\ =\ a\ -\ bM_L$ [*Gutenberg and Richter*, 1942], where a is constant that describes the total earthquake number and b describes the relative size distribution. Higher *b*-value indicates more small events and fewer large events. The G-R law and slight modifications thereof are used in essentially all seismic hazard studies [e.g., *Giardini et al.*, 2004] as it allows extrapolation from the observed smaller events to the infrequently observed larger ones. Studies of microearthquakes on faults [e.g., *Schorlemmer and Wiemer*, 2005] have shown that the

b-value, when mapped with high quality data at high spatial resolution, varies in the Earth's crust over distances of a few kilometers or less.

Method

The *b*-values determined in this study were calculated using the maximum likelihood *b*-value calculation subroutine in the ZMAP software package [*Wiemer*, 2001]. Rather than using the grid options provided in ZMAP; instead, we use the focus-centered mapping technique *in Bachmann et al.*, [2012] to map the 3D *b*-value distributions. Specifically, for each earthquake, I use 3D distance to search the nearest 150 events to calculative *b*-value instead of using only horizontal distance. Maximum-likelihood *b*-values were computed using the following equation [*Utsu*, 1965; *Aki*, 1965]:

$$b = \frac{1}{\bar{M} - M_{min}} log\ e\ , \tag{7}$$

where $\bar{M}$ is the mean magnitude and M_{min} the minimum magnitude of 150 chosen events used in b-value calculation.

The earthquake catalog is considered to be incomplete below a certain magnitude, which is generally taken to be the minimum magnitude M_{min}. I use the M_c to define the catalogue threshold for *b*-value estimation. And M_c has to be corrected by the half of magnitude interval $\Delta M/2$ to compensate the bias of rounded magnitudes to the nearest ΔM bin, thus $M_{min} = M_c - \Delta M/2$ [*Utsu*, 1965; *Guo and Ogata*, 1997)].

To account for potential spatial heterogeneity in M_c, I determine local M_c using the closest 150 events using the maximum curvature method [*Woessner and Wiemer*, 2005]. I then select closest 150 events above local M_{min} to determine the *b*-value with the maximum likelihood method [*Utsu*, 1999].

Result and discussion

The *b*-value map images (Figure 13) illustrates several interesting features:

1) A low *b*-value anomaly (red circle in Figure 13) near a group of $M_L \geq 2.5$ earthquakes, which may suggest existence of a pre-existing fault plane [*Wiemer and Wyss*, 1997; *Schorlemmer et al.*, 2004; *Goebel et al.*, 2013] or high differential stress [*Bachmann et al.*, 2012; *Amitrano*, 2003; *Schorlemmer and Wiemer*, 2005];

2) Relatively higher *b*-value near injection well zones (white squares in Figure 13), consistent with the previous observations of higher *b*-value in geothermal areas near the casing shoe [e.g., *Bachmann et al.*, 2012] due to pore-pressure changes [*Grünthal*, 2014];

3) Large earthquakes (magenta star in Figure 13) with magnitude larger than 4.0 from 1981-2007 mostly located in the deeper layers, correlating to an area with normal *b*-value (~ 1.1) (Figure 13b). There is no $M_L \geq 4$ event between 2008 and 2014 when the borehole stations are open access.

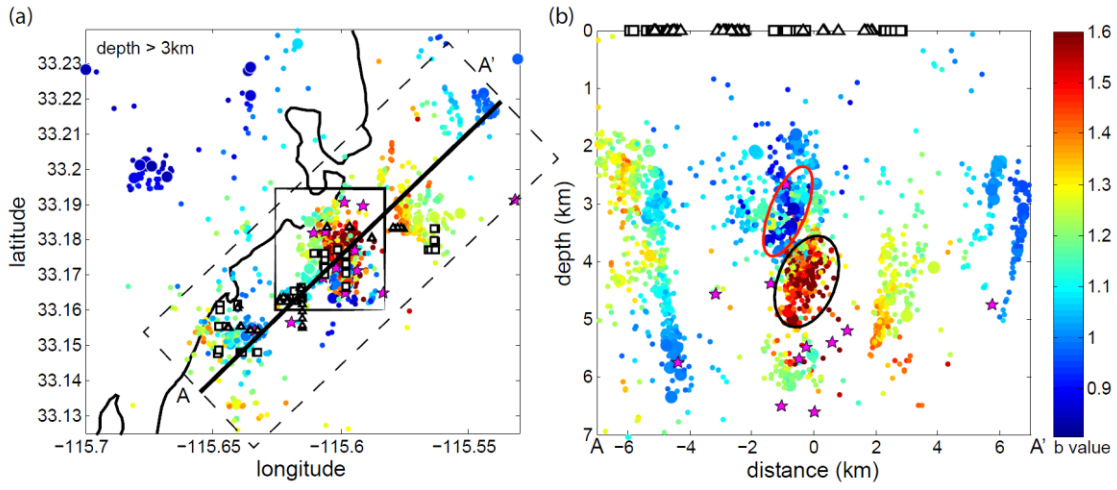

Figure 13. (a) map of the spatial variation of *b*-value, we only plot events with $\mathbf{3 \leq depth \leq 7}$. (b) cross-section (AA') view of events in dashed box. White square indicates injection well, white triangle is production well and magenta star shows historic large magnitude events with $\boldsymbol{M \geq 4}$ since 1981. Events with $\boldsymbol{M \geq 2.5}$ in our

study period are indicated by larger circle. Note the patch of high *b*-value in the middle area (3.5 – 5 km). Circles denote the low *b*-value anomaly area (red) and high *b*-value area (black). The solid line box is the chosen area for detailed discussion and the black contour shows the boundary of Salton Sea.

Large magnitude event (LME) probability distribution

Method

Wiemer [2000] and *Bachmann et al.* [2012] defined the probability p of an event exceeding a certain magnitude M as

$$p = 1 - e^{-\frac{1}{x}}, \tag{8}$$

Where

$$x = 1/(a - bM_L). \tag{9}$$

For each event, I use equation 9 and 10 to calculate the probability of event exceeding magnitude 3, where *a*-value and *b*-value are estimated based on closest 150 events. The probability of an event with $M_L \geq 3$ is shown in Figure 14.

Result and discussion

I find that the probability for LME ($M_L > 3$) is higher in area far from geothermal operation. And based on map view of LME probability (Figure 14a), the faults interpreted from the 2005 earthquake swarm (locations are based on the *Hauksson et al.*, [2012] catalog) separate their surrounding areas into low LME probability area and high LME probability. *Lohman and McGuire* [2007] calculated the static stress change caused by the inferred aseismic creep (red dash line in Figure 14) from the geodetic data. And they find that the aseismic creep cause positive stress change to its north-left part and negative stress change to its south left part. And our result is consistent to the inferred stress change with high LME probability at north left part of

aseismic fault, between the aseismic fault and main central fault that ruptured during the 2005 swarm (Figure 14b).

The spatial distribution generally shows relatively low probability of LME within the geothermal reservoir, and high probabilities outside the reservoir. The high probability areas within the geothermal field are mostly adjacent to the main central fault outlined by the 2005 earthquake swarm (Figure 14). The spatial coherent pattern suggests that tectonic faults likely impose greater earthquake hazards in the broader SSGF region.

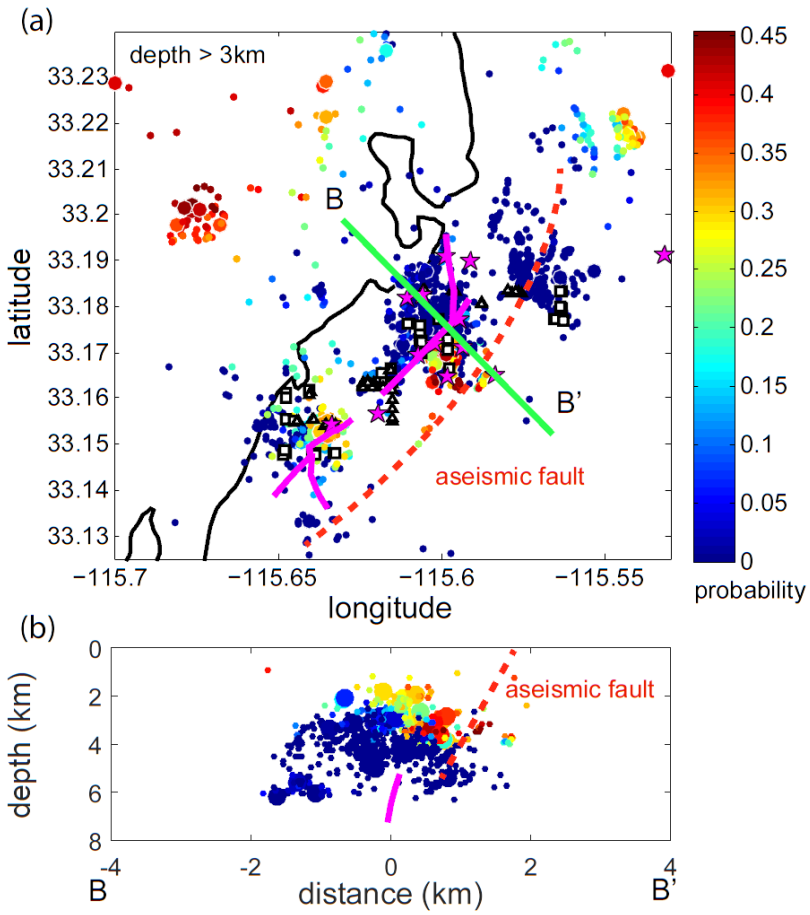

Figure 14. Event with $\boldsymbol{M_L \geq 3}$ (circle color) and $\boldsymbol{3 \leq \text{depth} \leq 7}$ km in (a) map view. Cross-section (b) BB' view of events and faults in a. White square indicates injection well, white triangle is production well and magenta star shows historic large magnitude events with $\boldsymbol{M_L \geq 4}$ since 1981. Events with $\boldsymbol{M_L \geq 2.5}$ in our study period are indicated by larger circle. The green line denotes the cross-section BB'. The magenta line is the main fault interpreted by 2005 swarm. The red dash line highlights aseismic fault from *Lohman and McGuire* [2007]. The black contour shows the boundary of Salton Sea.

Chapter 3. Stress drop analysis

Fundamental source properties for earthquakes can be estimated using far-field recordings of the P and S wave arrivals spectral content. One of the most important source parameters that can be computed is the stress drop, $\Delta\sigma$, which is the difference between the average state of stress on the fault plane before and after an earthquake [*Kanamori and Brodsky*, 2004].

Analyses of seismic networks enable us to investigate the spatial variations of stress drops in specific regions in order to understand the details of rupture characteristics. *Hardebeck and Aron* [2009] found that stress drop is controlled by the applied shear stress acting on the Hayward Fault. *Mukuhira et al.* [2010] studied spatial stress drop distributions found that most of the larger magnitude events occurred in regions of higher stress drop. Area of high stress drops could indicate potential nucleation zones for future moderate to large earthquakes [*Allmann and Shearer*, 2007].

In this study, I estimate the stress drops of a large amount of earthquakes in the SSGF using data recorded by the local borehole seismic network and Empirical Green's Function method. The detailed spatial variation of stress drop will help us to understand spatial variations in fault properties and explore its relation to fluid injection.

Stress drop estimation method

Data processing

I require the earthquakes to have picked P wave arrivals at five or more stations. I compute displacement spectra of short period instruments using the multitaper method of *Park et al.* [1987] using a 0.5 s time windows before (noise) and after (signal) the picked P and S arrivals. I require a signal-to-noise amplitude ratio of at least 3 between

3-10 Hz and 10-15 Hz frequency bands and 2 between 15-20 Hz for all spectra. I also require each event to be recorded at this signal-to-noise level by at least five different stations. This restriction is intended both to better isolate station effects, and to average out directivity effects, which can affect the source parameter estimation [*Venkataraman and Kanamori*, 2004].

I apply the spectral analysis method described by *Shearer et al.* [2006] to this data set. In the logarithmic frequency domain, the observed displacement spectrum, $d_{ij}(f)$ of the source i and receiver j can be described by a linear combination of a source term e_i, a receiver term s_j and a traveltime-dependent term $t_{k(i,j)}$:

$$d_{ij} = e_i + s_j + t_{k(i,j)} + r_{ij}, \tag{10}$$

where r_{ij} is a residual term. Based on equation (10), we separate the source term e_i of the displacement spectra by means of an iterative robust least squares approach [*Shearer et al.*, 2006]. I estimate the relative seismic moment Ω_0 of each event from the amplitude of the low-frequency ($1-3$ Hz) part of the isolated source term $\boldsymbol{e}$. We calibrate the measured relative seismic moment Ω_0 to the absolute moment M_0 using the local magnitude M_L by fitting a linear relationship between $log(\Omega_0)$ and M_L following:

$$M_L = 0.87\, log_{10}\, \Omega_0 + 1.01 \tag{11}$$

(Figure 15).

The resulting relative source spectra need to be corrected by an empirical green's function (EGF) to correct common propagation effects before estimating source parameters for individual events. Here we use the stack-and-invert method of *Shearer et. al* [2006] to correct the relative source spectra.

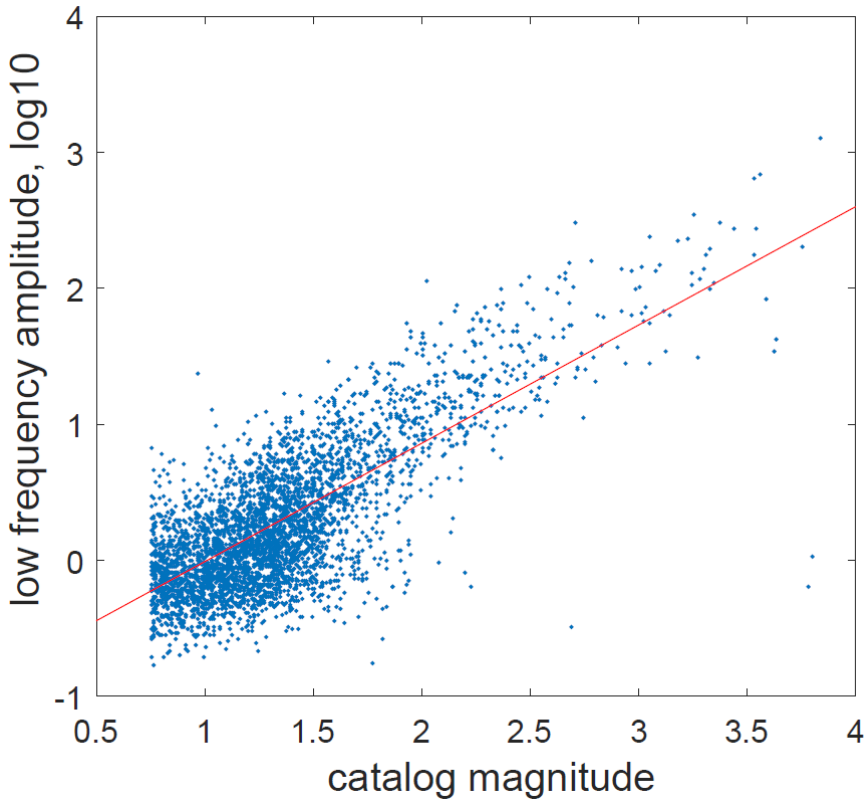

Figure 15. Empirical estimate of low-frequency (1-3 Hz) amplitude, $\boldsymbol{\Omega_0}$, versus local magnitude $\boldsymbol{M_L}$. Blue dots represent individual event. Regression line is shown in red.

Empirical Green's Function Method

To account for spatial variations in propagation effects, I divide the whole area into 5 sub-areas (Figure 16), based on the event distribution and geothermal operation well location. For each of the 5 sub-areas, I follow the process described in *Shearer et al.*, [2006] to obtain the EGF. I first stack event spectra in 0.2 magnitude bin. Figures 18a and b show the stacks for two example regions. Each stacked spectrum is assumed to follow the ω^{-2} model [*Brune*, 1970] (Figure 17) with an average stress drop. The displacement spectrum, $u(f)$, is then

$$u(f) = \frac{\Omega_0}{1+(f/f_c)^2}. \quad (12)$$

Assuming a circular fault surface, with radius r_{radius}, the stress drop $\Delta\sigma$ can be calculated from the seismic moment M_0 and the source radius r_{radius} [*Eshelby*, 1957]:

$$\Delta\sigma = \frac{7}{16}\left(\frac{M_0}{r_{radius}^3}\right). \quad (13)$$

The source radius r_{radius} can be related to the corner frequency following the *Madariaga* [1976] relation:

$$f_c = 0.32\frac{\beta}{r_{radius}}, \quad (14)$$

where β is the shear wave velocity near the source. In this study, I use the 3D P-wave velocity model in *McGuire et al.* [2015] to estimate in-situ shear wave velocity with a constant Vp/Vs ratio of 1.732. Combining equations (13) and (14), I obtain

$$\Delta\sigma = M_0\left(\frac{f_c}{0.42\beta}\right)^3. \quad (15)$$

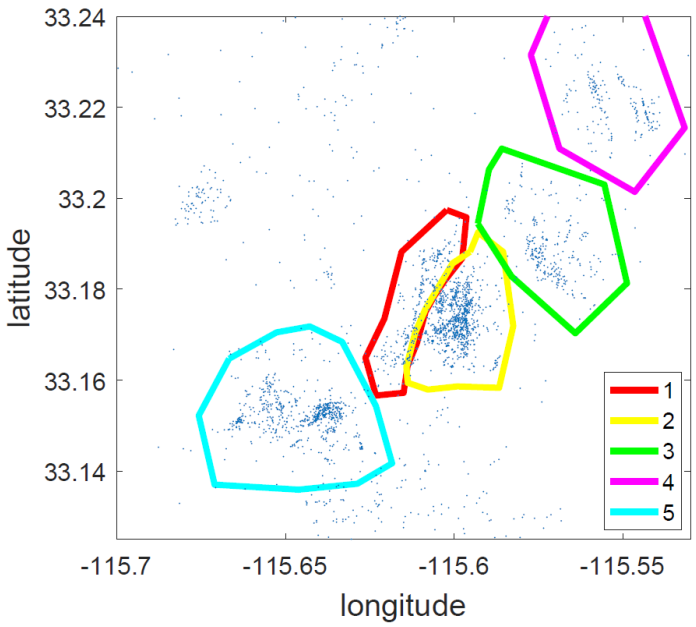

Figure 16. Selected regions for stress drop estimation. For each region, I compute a single Empirical Green's Function (EGF) computed from the stacked the events spectra terms and use it to correct spectra.

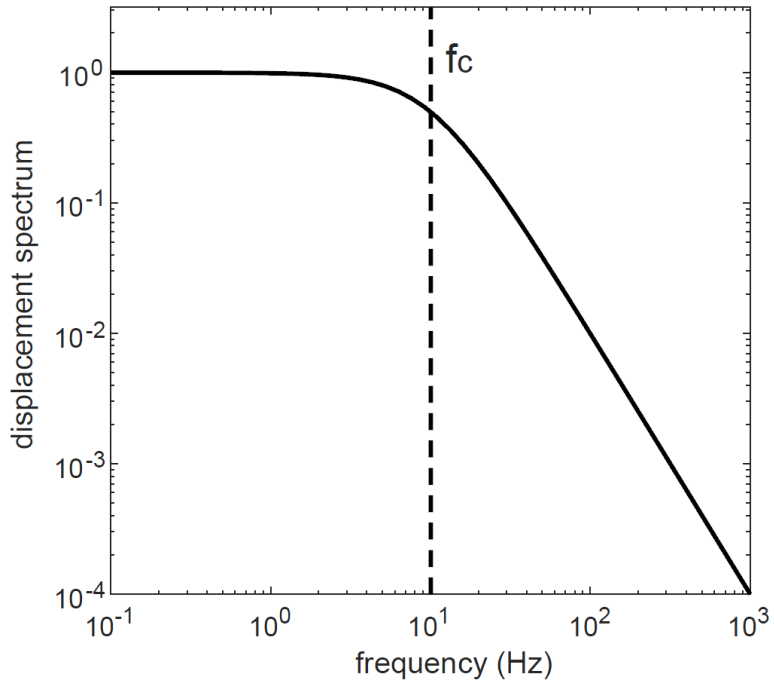

Figure 17. Spectra of Brune model [*Brune*, 1970] with corner frequency 10 Hz. The dashed line denotes the corner frequency.

The EGF is obtained by averaging the misfit between individual stacked spectra for each magnitude bin, and predicted theoretical spectra based on the source model and a constant stress drop. The best-fitting stress drop for each subarea is found by minimizing the overall misfit between observation and prediction over moment magnitude range from 0.62 to 1.29 (Figures 18c and d). Below and above this magnitude range, the number of events per magnitude bin is too small to obtain a stable estimate of the EGF. Figures 18e and f shows the EGF-corrected source spectra for the two example events.

After correcting the individual source spectra by subtracting the EGF for each subarea, I compute the stress drop from the best fitting corner frequency using equation (12) for individual earthquakes. I obtain the corner frequency from a least-squares fit of the deconvolved log spectrum with theoretical spectrum between 2 and 20 Hz. Corner

frequencies above the fitting range can be resolved with reduced accuracy [*Allman and Shearer*, 2007]. However, it is necessary to include these events for interpreting spatial patterns, as patches with high average stress drop will be otherwise excluded.

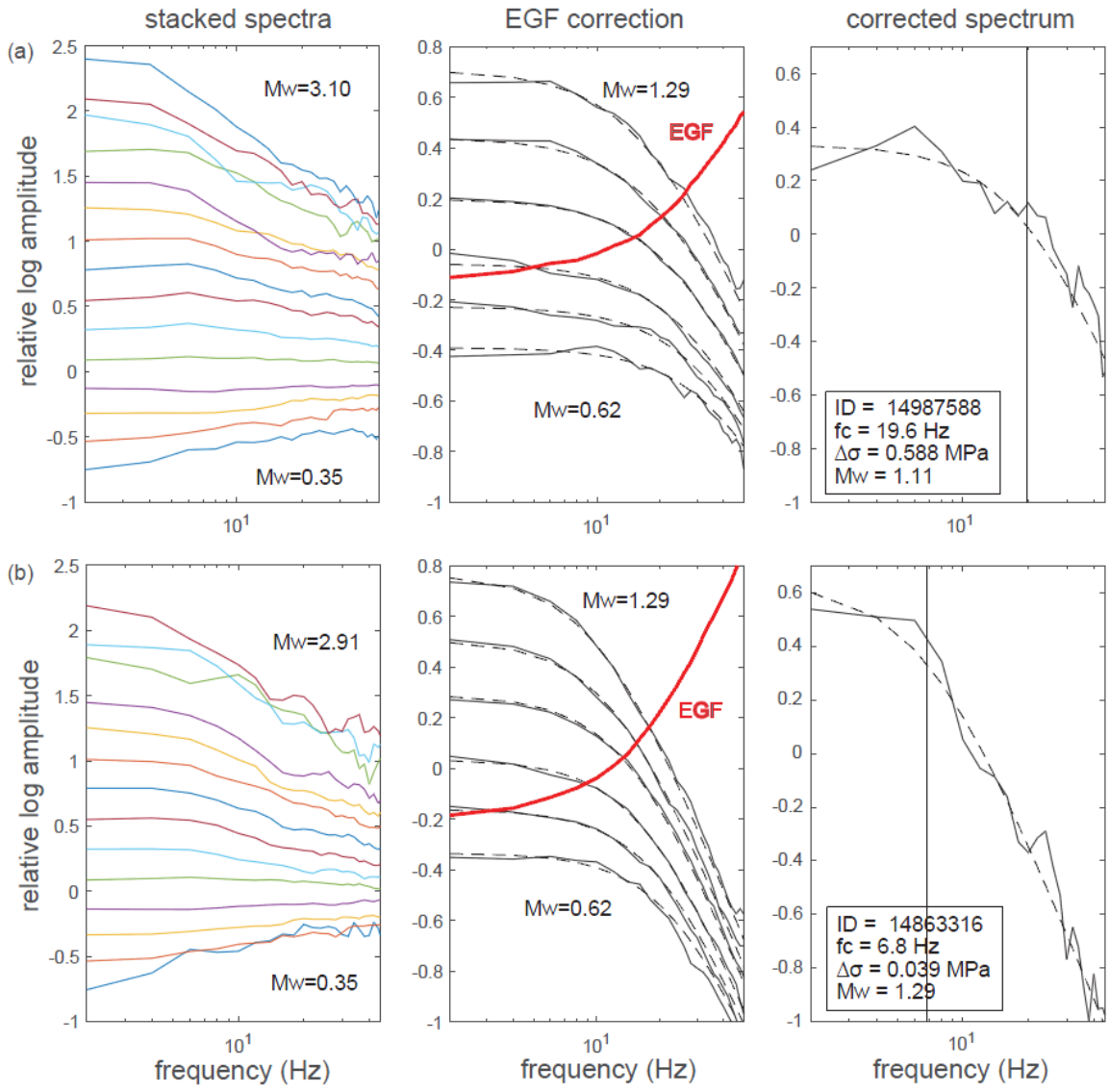

Figure 18. Two example events: (upper) one for a medium stress drop region (region 2 in Figure 17) and (lower) one for a low stress drop region (region 5 in Figure 17). The SCSN cuspid numbers are 14987588 and 14863315, respectively. (a, d) Stacked source spectra in 0.2 local magnitude increments over 200 events. The lower and upper moment magnitude bounds are marked. (b, e) EGF-corrected spectra (solid) in comparison to theoretical spectra (dashed). The bold red solid curve shows the EGF, which was computed over a moment magnitude range from 0.62 to 1.29. (c, f) EGF-corrected source spectra of the respresentative target event (solid) together with the best

fitting theoretical spectrum (dashed). The corner frequencies in Hz are indicated as numbers along the curves. The best fitting corner frequencies $\boldsymbol{f_c}$ and resulting stress drops $\boldsymbol{\Delta\sigma}$ are also indicated.

I obtained stress drop estimates for 1954 earthquakes with corner frequencies ranging between $1 - 50$ Hz. The absolute values of stress drop could be affected by the assumption of a circular crack, the assumed relation between crack radius and corner frequency, the derived rupture velocity in equations (14) and (15), and the EGF correction, where different choices could shift these stress drop values systematically higher or lower. However, because the same assumptions were made for each earthquake, the relative variations should be robust.

The $\Delta\sigma$ estimates follow a typical log-normal distribution, with values varying over more than two orders of magnitude with a median $\Delta\sigma$ of 0.23 MPa (Figure 19a), similar to the estimates of *Chen and Shearer* [2011] for the same region, but significantly lower than the rest of Southern California and the Parkfield section [*Shearer et al.,* 2006; *Allmann and Shearer,* 2007]. High heat flow in the Salton Trough is a likely cause as other studies also observe relatively low stress drops within geothermal areas, i.e., the Coso geothermal field and triggered earthquakes within the Salton Sea geothermal field [*Hough et al.*, 1999; *Hough and Kanamori*, 2002].

Previous observations show that both natural seismicity [e.g., *Abercrombie*, 1995; *Allmann and Shearer*, 2009] and for induced seismicity [e.g., *Sellers et al.*, 2003; *Kwiatek et al.*, 2010] are with scale-invariant $\Delta\sigma$ is scale-invariant. I do not observe an obvious scaling of $\Delta\sigma$ with magnitude over the available M_w range, suggesting that self-similarity also holds for the induced seismicity in the SSGF (Figure 19b). To test the robustness of obtained result, I use bootstrap resampling with replacement over 100

iterations and computing 95% confidence interval of obtained median values for each magnitude bin.

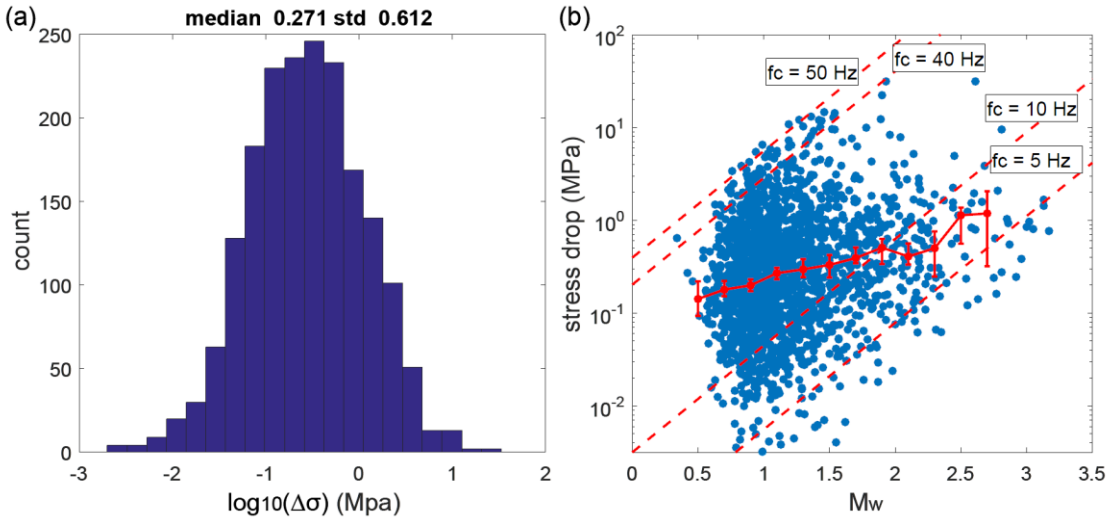

Figure 19. (a) Histogram of log stress drop for 1954 events, with corner frequency in the range 1-50 Hz. (b) Stress drop versus moment magnitude. Dashed lines show constant corner frequencies as marked. And the red solid line shows median stress drop per magnitude bin with standard errors (vertical error bar) from 100 iterations bootstrap resampling. The apparent trend of stress drop with magnitude is therefore clearly an artifact of the limited frequency band.

In order to examine large-scale variations of the stress drops in space, for each earthquake location, I bin the median stress drops, rather than take an average, as the estimated stress drop to provide representative stress drops, since the median is less affected by outliers. I first project events onto map and cross-section AA' respectively. Then I calculate the median value of stress drops in each space bin, and use a median filter to smooth the result. The spatial distribution of the stress drops obtained using constant EGF are shown in Figure 20.

Examining Figure 20a, there is no clear correlation between injection well location and median stress drop. The central area exhibits a higher averaged stress drop near injection well compared with other areas. From the cross section along AA' (Figure

20b), there is increasing stress drop with depth is clear in regions 3, 4 and 5 (right and left side of black square in Figure 20b), but a decreasing of stress drop with depth in regions 1 and 2 (black square in Figure 20b). A high stress drop is located in the middle area at about 2-3 km depth.

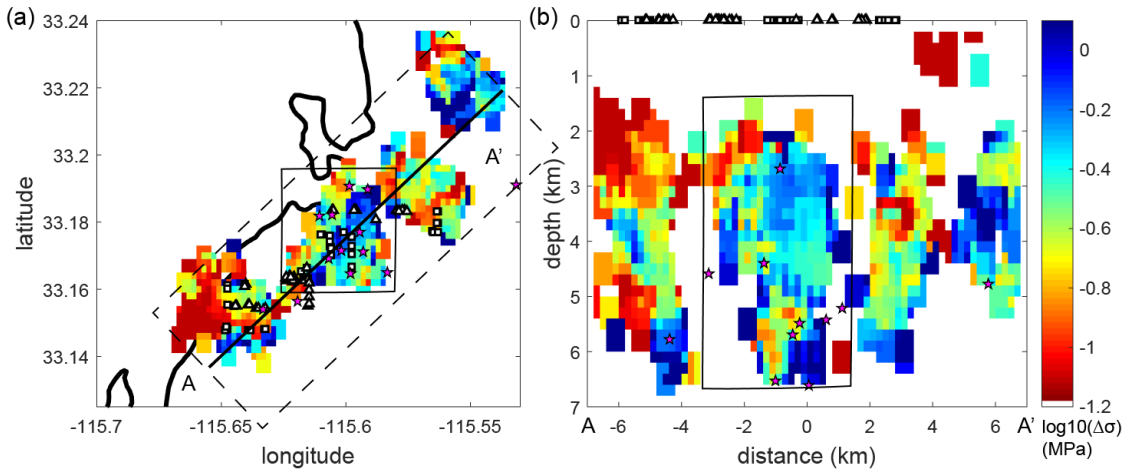

Figure 20. (a) Map view of the median stress drops for individual earthquakes in $\mathbf{0.002°} \times \mathbf{0.002°}$ bins, smoothed using a moving median window of $\mathbf{0.006°} \times \mathbf{0.006°}$. (b) Cross-section view of the median stress drops for individual earthquakes within the dashed line box, shown projected onto the solid line AA'. Median stress drop in $\mathbf{0.02km} \times \mathbf{0.02km}$ bins, smoothed using a moving median window of $\mathbf{0.06km} \times \mathbf{0.06km}$. The solid line box is the chosen area for detailed discussion and the black contour shows the boundary of Salton Sea.

Depth dependence

Many observations indicates an increase of stress drop with depth [e.g., *Jones and Helmberger*, 1996; *Hardebeck and Hauksson*, 1997; *Venkataraman and Kanamori*, 2004]. In Southern California, *Shearer et al.* [2006] observe an increase of median stress drop from 0.6 MPa near the surface to 2.2 MPa at 8km depth with assumption of a constant rupture velocity. However, *Allmann and Shearer* [2007] observe that estimating stress drop using depth-varying shear wave velocity can attenuate depth dependence of stress drop. For our study, we have already used depth-varying shear

wave velocity from high resolution 3D velocity model in *McGuire et al.* [2015]. It is very unlikely that the shear wave velocity errors exceed 25% according to the tomography studies; uncertainties in velocity cause stress drop errors of less than a factor of 2, much less than the observed nearly an order of magnitude variation in stress drop with depth. Therefore, the overall depth dependency of the stress drop cannot be purely due to processing artifact. A possible contributor to the increase of stress drop with depth in region 3, 4 and 5 is the increased fault strength with increased confining pressure. In contrast, the stress drops in region 1 and 2 decrease with depth. For shallow area (1 – 3 km depth), the median value of stress drops vary dramatically. But the median value of stress drop does not change significantly from 3 to 5 km depth.

Repeating earthquakes

While the median value of static stress drop $\Delta\sigma$ is almost constant over several orders of magnitudes (Figure 19b), the stress drop varies over two orders of magnitude. It is unclear if this stress drop is purely due to measurement errors or if it reflects the variability of earthquake rupture processes. To address this uncertainty, I analyze the stress drop of closely located earthquakes with similar waveforms.

Identification of repeating events

I search for the repeating earthquakes with high waveform similarity. I first measure the cross-correlation coefficient between each earthquake and its nearest 500 earthquakes, using time windows of -0.3s before and 0.8s after the P-wave arrivals in the frequency range 10-40 Hz. If the cross-correlation coefficient is larger than 0.9 recorded by at least two stations, the two earthquakes are “linked” and regarded to be part of the same repeating group. I find a repeating group with 15 events, which have

similar waveforms recorded at multiple borehole stations (Figure 21). All the events in this repeating group are within a few hunderds of meters of each other both horizontally and vertically (Figure 22), suggesting that they may occur on the same fault patch.

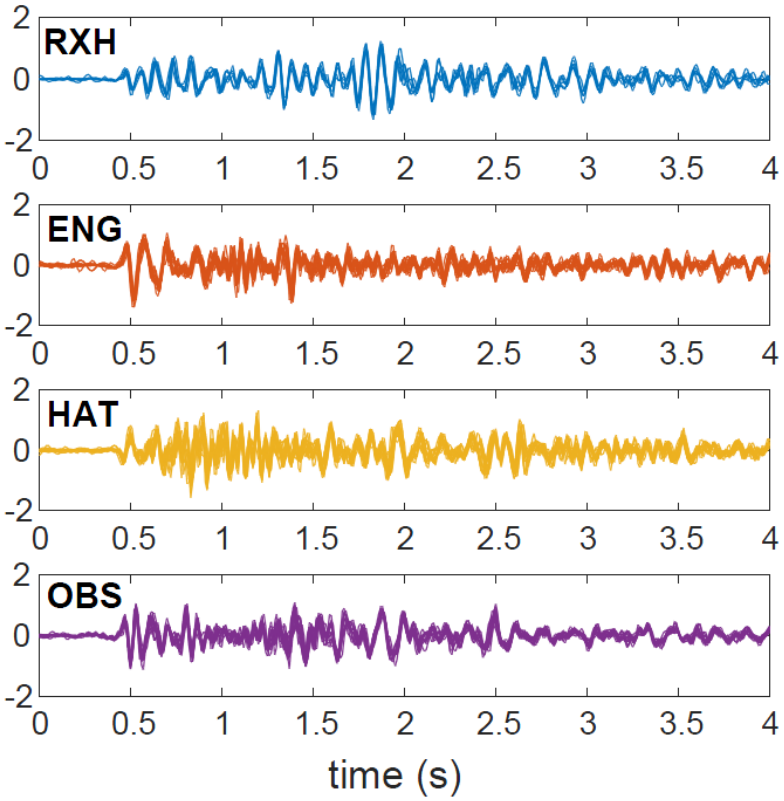

Figure 21. Waveforms recorded on the vertical component sensor at various station sites for the selected repeating events. The waveform of each event is normalized by its maximum amplitude. All waveforms have been aligned on the P wave arrival and are filtered in the range 10–40 Hz. Note the high similarity of the waveforms after 3 s for all groups. Station names are identified in the upper left corner.

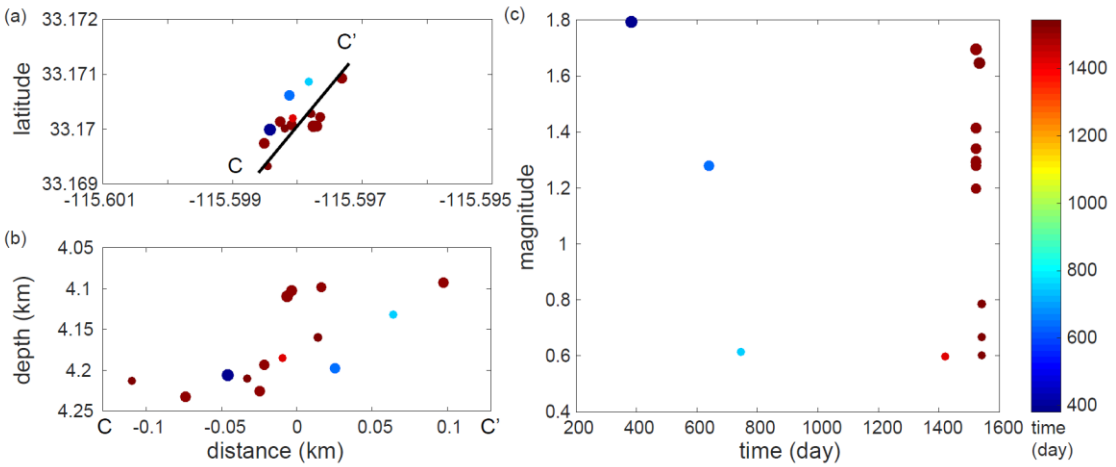

Figure 22. (a) Map view and (b) cross section CC' view of events in the repeating group. (c) Scatter plot of magnitude and time of events in the repeating group. The events are colored by time and their sizes are proportional to event size.

Relative moments

Despite using highly similar waveforms and locations, events in repeating group can still have large amplitude variations. Two events with magnitude 1.6 and 0.6 (event No.6 and No. 13 in Table 1) have very similar waveform shape but exhibit relative amplitude differences by factors of 2 to 11 (Figure 23). This variation reflects the large difference in the waveform amplitudes that can exist from repeating events, which can be directly related to a variation of moment, M_0^r. For repeating events recorded at each station, we first align the waveforms of all events and use the waveform between 0.2s before and 3.8s after P wave arrival time to perform the singular value decomposition (SVD) approach. This method compares the amplitude of the first output basis vector (resulting from SVD), provide a more precise estimate of amplitude differences less affected by noise.

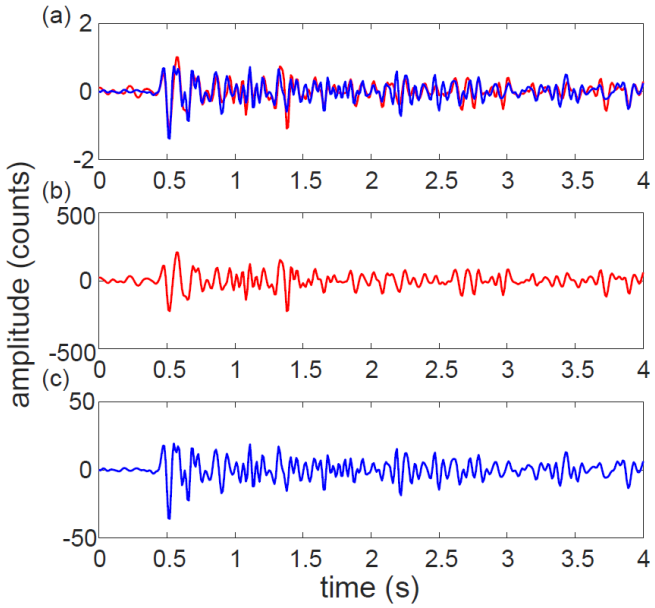

Figure 23. Waveforms recorded at the same station (ENG) for the two events in the repeating group. (a) Seismogram of event No. 6 (red) and event No. 13 (blue) in table 1 with normalized amplitude. The seismogram with original amplitude of event No. 6 (b) and event No. 13 (c) in Table 1.

Table 1. Detailed relative stress drop of events in the repeating group

Event number	event id	time (day)	radius (m)	M_0^r	$\Delta\sigma_0^*/\Delta\sigma^*$	$\Delta\sigma_0/\Delta\sigma$	M_L
1	10371581	381.254	77.252	0.13848	7.22	11.67	1.7
2	14520852	641.419	75.844	0.2053	4.87	7.45	1.2
3	10529437	746.073	70.418	0.26691	3.75	4.58	0.6
4	11035445	1421.786	85.378	0.08445	11.84	25.83	0.5
5	15117793	1524.052	73.165	0.18427	5.43	7.45	1.2
6	**37028531**	**1524.097**	**65.835**	**1.00000**	**1.00**	**1.00**	**1.6**
7	15117833	1524.096	78.313	0.79817	1.25	2.11	1.4
8	15117857	1524.102	76.112	0.19023	5.26	8.12	1.2
9	15117865	1524.104	64.721	0.26216	3.81	3.62	1.3
10	15117889	1524.118	80.936	0.42512	2.35	4.37	1.1

11	15118049	1524.25	61.498	0.19895	5.03	4.1	1.2
12	11079538	1533.818	80.197	0.21393	4.67	8.45	1.6
13	11082386	1541.079	70.571	0.14551	6.87	8.47	0.6
14	11083282	1543.073	76.837	0.3312	3.02	4.8	0.6
15	11083346	1543.096	77.279	0.3106	3.22	5.21	0.7

Event time is measured in day since 1 January 2008. The rupture dimension is estimated using event No. 6 with radius of r = 65.835 m. And M_0^r is the relative moment compared with event No. 6. The first variation of stress drop $\Delta\sigma_0^*/\Delta\sigma^*$ assumes that all events have the same source radius. The second variation of stress drop $\Delta\sigma_0/\Delta\sigma$ accounts for size variation. All stress drop variations in the table are relative to the stress drop of event No. 6 in the group ($\Delta\sigma_0^*$ and $\Delta\sigma_0$). M_L is the catalog magnitude. The reference event is shown in bold face.

Source dimension estimation

Similar waveforms indicate that repeating earthquakes have similar source spectra (Figure 24) and rupture dimension. However, we still need to consider the variations in rupture area and compare them with the moment magnitude variation. I first compute the rupture size of event No.6 (in Table 1) in the repeating group using its deconvolved event term corrected by constant EGF in region 2. The corner frequency of the largest event is 15.1 Hz. The estimated source radius and stress drop of the largest event is 65.8 m and 1.0 MPa, respectively.

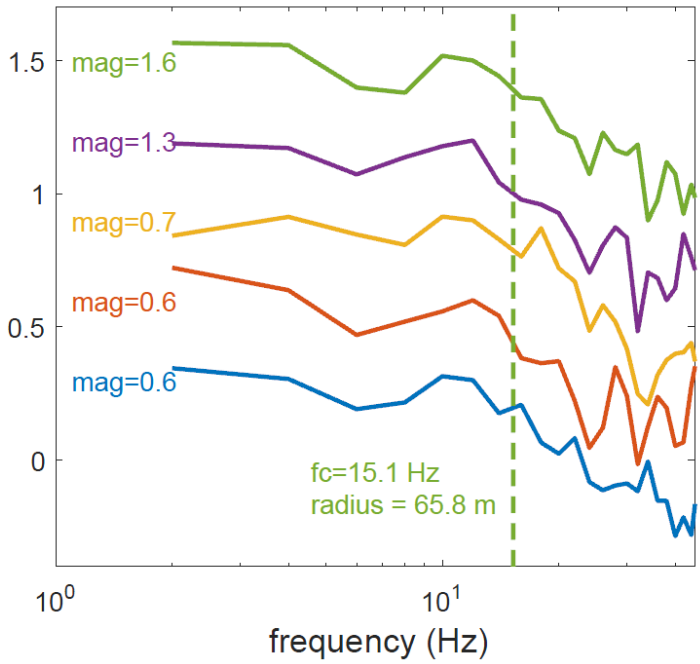

Figure 24. EGF-corrected source spectra of the respresentative events in repeating group. Spectra have been shifted vertically to enhance visibility. The dashed line highlight the corner frequency of the largest event in the repeating group.

Because of high waveform similarity, instead of estimating the corner frequencies individually, I estimate the corner frequency of the other events relative to the largest event in the repeating group using a spectral ratio approach [*Lengliné et al.*, 2014]. For closely located earthquake, the spectra ratio for records at the same station will suppress all propagation and station terms, leaving only relative source information between two events. Thus, I use the spectra ratio, $G(f)$,

$$G(f) = \frac{\overline{X(f)Y^*(f)}}{\overline{Y(f)Y^*(f)}}, \tag{16}$$

which relates the Fourier spectrum of the processed event x, $X(f)$ and event y, $Y(f)$ as performed in *Lengliné and Got* [2011]. $X(f)$ and $Y(f)$ are estimated using the displacement waveform with normalized amplitude recorded at each station on a long time window between 0.1s before and 2.4s after P wave arrival. Spectral densities are

smoothed by the Fourier transform of a Hanning window. Assuming a circular crack Brune model [*Brune*, 1970; *Madariaga*, 1977] (equations 12 and 14), the corner frequency of event x, f_{c1} and event y, f_{c2} yield

$$ln[G(f)] = \alpha + ln\left[\frac{1+\left(\frac{f}{f_{c2}}\right)^2}{1+\left(\frac{f}{f_{c1}}\right)^2}\right] \quad (17)$$

where α is the ratio of the low-frequency spectral level. If $f_{c1} = f_{c2}$, the spectral ratio is flat over entire frequency range (Figure 25a). With the increasing difference between f_{c1} and f_{c2}, the spectra ratio line shows increasing slope in the interval $[f_{c1}, f_{c2}]$ (Figures 25b and c).

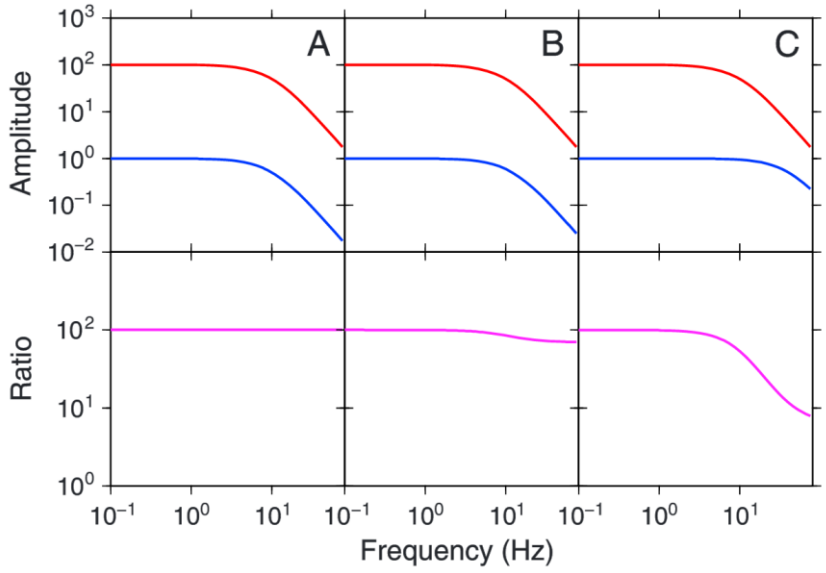

Figure 25. Scheme depicting three different cases of earthquake pairs. For each case we represent the P wave displacement spectra of the (top) two events and (bottom) their spectra ratio. (a) The two earthquakes have the same corner frequency but different amplitudes. The spectral ratio is flat over the entire frequency range. (b) The two earthquakes have almost the same corner frequency and different amplitudes. The spectral ratio can be well fitted by a linear function around the corner frequency of the two events. (c) In the third scenario, the two earthquakes have two different amplitudes and different corner frequencies. In this case the spectral ratio is not flat anymore and we expect a transition between the corner frequencies of the two events. From *Lengline et al.* [2014].

I use the method proposed by *Got and Fréchet* [1993] to extract the variation of rupture dimension between two events, assuming $f_{c1} \cong f_{c2}$, and the difference between the corner frequency of the first and second event is $\Delta f_c = f_{c1} - f_{c2}$. Then the slope of $ln[G(f)]$ can be written as

$$slope = \frac{d(\,ln[G(f)])}{df} = 2f\,\frac{f_{c1}^2 - f_{c2}^2}{(f_{c2}^2 + f^2)(f_{c1}^2 + f^2)}. \quad (18)$$

When f_{c0} is close to f_{c1} and f_{c2}, then slope of $\ln[\mathrm{G}(\mathrm{f_{c0}})]$ follows that

$$slope = 2f_{c0}\,\frac{(f_{c1} - f_{c2})(f_{c1} + f_{c2})}{4f_{c0}^4} = 2f_{c0}\,\frac{2f_{c0}(f_{c1} - f_{c2})}{4f_{c0}^4} = \frac{\Delta f_c}{f_{c0}^2}. \quad (19)$$

The slope can be related to the radius of the rupture size by using equation (14) with the assumption $f_{c1} \cong f_{c2}$, which gives

$$\frac{\Delta f_c}{f_{c0}^2} = \frac{\Delta \mathrm{r}}{0.32\beta}, \quad (20)$$

and is equivalent to

$$\Delta r = 0.32\beta * slope. \quad (21)$$

For each spectral ratio at each possible station, I performed a linear fit on $ln[G(f)]$ in the frequency range 10-40 Hz, corresponding to the range with high waveform similarity. The best-fit line provides us an estimate of $slope$ which can be translated into Δr. Finally, I determine the relative source radius for each event in the group. For example, the radius difference between these two events in Figure 26 at all stations is only several meters. The average variation of $|\Delta \mathrm{r}|$ computed over all events relative to the largest events in the group is 7 m (Table 1). It suggests that all events in the repeating group have the similar source dimension. The relative variation of rupture size is much smaller than the rupture size.

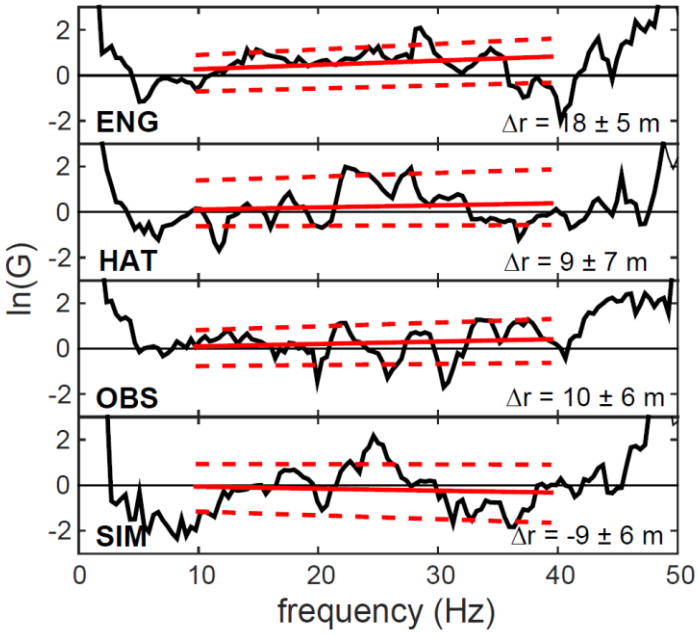

Figure 26. Black lines represent logarithm of the spectra ratio between two events No. 6 and No. 13 in the repeating group computed at several stations using equation (16). The linear fit of $\boldsymbol{ln}[\boldsymbol{G}(\boldsymbol{f})]$ in the frequency ranging from 10 Hz to 40 Hz, where we have similar waveform, is indicated by the two red lines. They represent the 95% confidence interval of possible fits. The associated variation of rupture dimension, $\boldsymbol{\Delta r}$ between the two events computed at each station is indicated.

Variable stress drop events

Based on equation (15), the stress drop variations between two events can be obtained as

$$\frac{\Delta\sigma_1}{\Delta\sigma_2} = \frac{M_{01}}{M_{02}}\left(\frac{r_{radius2}}{r_{radius1}}\right)^3. \quad (22)$$

Because all events in the repeating group have similar source dimension, the areas A are also similar for those events. Then based on

$$M_0 = \mu AD, \quad (23)$$

the variation of seismic moment M_0 can be interpreted as the variation of seismic slip D and shear modulus μ. If the shear modulus is regarded as constant with time at the

location of a repeating group, then the relative variation in resolved seismic moment reflects the variation of both seismic stress drop and seismic slip.

Discussion

Although events in the repeating group seem to have similar rupture sizes, their large moment differences indicate a large variation in stress drop.

Combining equations (14) and (15), the stress drop can be represented as

$$\Delta\sigma = \frac{7 f_c^3 M_0}{16(k\beta)^3}. \quad (24)$$

Based on equation (24), the stress drop variation can be attributed to the variation of corner frequency f_c, seismic moment M_0 or shear wave velocity β. As discussed above, events in the repeating group have very similar waveform with cross-correlation coefficient larger than 0.9. From Figure 24, the corner frequency variations between these events are too small compared with the estimated corner frequency of the largest event (15 Hz). I assume constant rupture velocity among the repeating events. Although earthquake rupture velocity variations have been observed, it is generally limited in a narrow range between 0.7 β to 0.9 β [*Kanamori and Brodsky*, 2004]. This variation is not large enough to compensate for the variation of moment observed in our study. The assumption of a constant stress drop requires a change of rupture velocity by a factor of $\sqrt[3]{11}$=2.2 to compensate a factor of 11 of amplitude difference between two events. For this reason, the relative moment variations are more likely related to the variation of seismic slip and static stress drop than to velocity.

I also observe that there are six events (events No.5-No.10 in Table 1) in the repeating group occurring in only 5 hours and these seven events are in the same mixture-type cluster. The largest variation of stress drop among these events is a factor

of 5.43. This suggests that the stress drop variations are caused by a local short-term rapid stress perturbation instead of a regional long-time process, which is consistent with the conclusion that the mixture-type cluster is mainly related to injection in my study. Other of induced seismicity studies in geothermal fields found local fluctuations of the stress drop related to pore pressure perturbation caused by injection [*Goertz-Allmann et al.*, 2011; *Chen and Shearer*, 2011; *Lengline et al.*, 2014]. The local fluid fluctuation can be caused by various reasons, for example: increased permeability due to newly created fractures by earthquake rupture [*Neuville et al.*, 2010]; or volume changes due to slip on the interface that changes the amount of trapped fluid.

Chapter 4. Discussion and Conclusion

Seismicity in relation to geothermal operations

Due to a lack of detailed knowledge of the penetrate depths of the injection and production wells, it is difficult to obtain a definite link between seismicity characteristics and individual injection wells as in the cases with hydraulic fracturing induced seismicity [e.g., *Bachmann et al.*, 2012]. The deepest injection well extends to about 2.2 km depth, which is shallower than most earthquakes in this region [*Hulen et al.*, 2003]. It is possible that the absolute depth may shift systematically, as we lack a good resolution for a velocity model shallower than 1 km [*McGuire et al.*, 2015]. Because of these uncertainty factors, I focus on the lateral relationship between seismicity and geothermal wells, and the relative spatial coherency of seismicity characteristics.

Based on the event size and the lateral distance to the nearest injection and production well, the events shows a bimodal distribution (separated by red lines in Figure 27), suggesting that geothermal operation can influence the seismicity distribution: earthquake within the geothermal field (distance < 3km from wells) is different from those outside the geothermal field (distance > 3km from wells). These two groups have similar amounts of large magnitude events ($M_L > 3$), while there are significantly more small magnitude events within the geothermal field compared with outside areas. Moreover, there is a cluster of microearthquakes ($M_L < 1.6$) located around 0.3 km to injection wells, and 1 km to production wells (Figure 27). The shorter distance and tighter clustering around injection wells compared with production wells suggest that fluid injection is more likely to induce earthquake compared with fluid

extraction. The frequent fluid perturbation near injection wells may reduce normal stress on pre-existing fractures [*Reyners et al.*, 2007] or cause high stressing rates in the surrounding rock [*Soosalu et al.*, 2010] and induce those microearthquakes. The magnitude-distance density plot is consistent with the event-size-frequency distributions with higher *b*-value closer to injection wells and higher LME probability outside the geothermal field. It is interesting to note that the largest magnitude decreases gradually with increased horizontal distance to nearest injection well (Figure 27a), although the cause is unclear.

For the earthquakes between 2008 and 2014, within the geothermal field, there is a combination of all three types of clusters, and they do not define clear fault trends. The concentration of mixtures near injection wells suggest that this area have some rupture processes mainly caused by local short-term stress change instead of regional stress loading. In contrast, outside the geothermal field, earthquakes tend to occur as individual aftershock or swarm sequences, and define clear fault trends that are consistent with expected fault orientations in the tectonic setting [*Chen and Shearer*, 2011]. Moreover, the *b*-value has a wider range (from 0.8 to 1.6) within the geothermal field, but is predominantly on the lower end (~0.9) outside the field, close to typical *b*-value in typical tectonic regions [*Nuannin*, 2006]. The high *b*-value and high intensity of small earthquake near injection well suggests short inter-seismic periods and lower accumulated strain energy released from individual earthquake. So I interpret the result of mixtures and high *b*-value near injection wells as the result of a reduced effective normal stress caused by the increase of fluid pressure during injection.

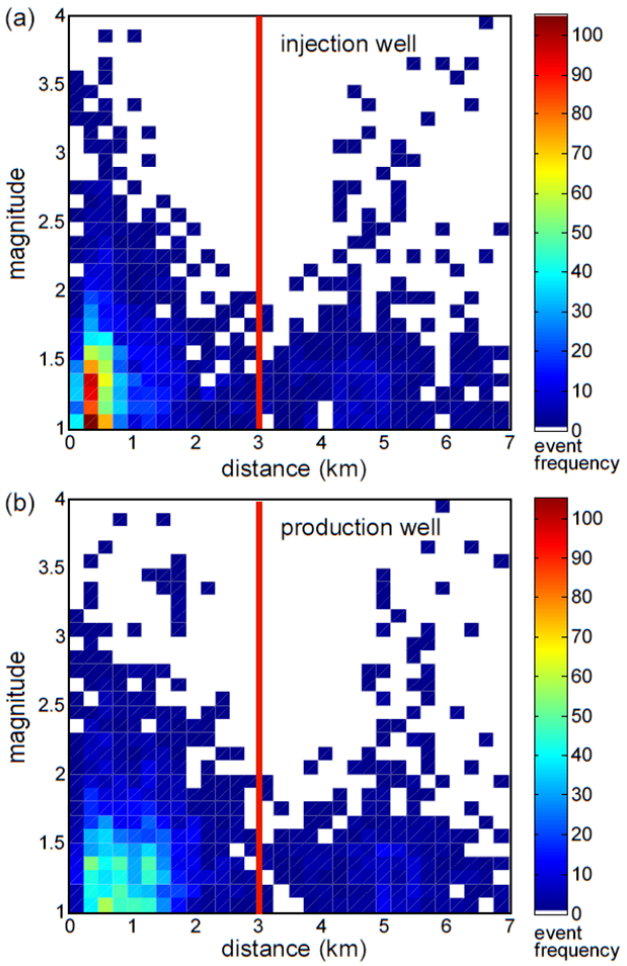

Figure 27. 2D histogram of event density per magnitude and distance relative to nearest (a) injection wells and (b) production wells. The events can be clearly divided into two groups depending on the distance to nearest well (red line).

Seismicity in relation to geological context

Focusing on the middle zone (Figure 28a), which has the best azimuthal station coverage from the borehole network and hosts the majority of events during the study period, I find that the *b*-value gradually changes. It has low *b*-value at the shallow layer in the south, and high *b*-value at deeper layer beneath production wells in the north, which decreases outside the 400°C/km geothermal gradient contour. Also the stress drop transits from high to low with the increasing depth, which is inversely correlated to

b value variation (i.e., high stress drop in areas with low *b*-value, vice versa). This is consistent with observations in the Basel geothermal field [e.g., *Goertz-Allmann et al.*, 2011; *Bachmann et al.*, 2012]. The two selected areas in Figure 28b clearly show significant differences in magnitude frequency distribution (Figure 29). The transition from low to high *b*-value is correlates with low temperature to high temperature; and injections wells with cold brine to production wells extracting hot brine, respectively. Note that some wells are not straight at depth, so the surface location may be slightly different from the location at injection depth [*Hulen et al.*, 2003]. Swarm and aftershock sequences occur in the low *b*-value, high average stress drop region with $M_{main} \geq 3$, and mixtures occur within high *b*-value and low average stress drop region with $M_{main} < 3$.

Although injection activities increase seismicity rates, felt events will not arise without suitably oriented fracture zones or faults under a critical stressed state [*Davis and Frohlich*, 1993]. Based on shallow thermal gradient distribution, the spatial variability of seismic characteristics in the middle field is strongly correlated with the distance relative to the intrusive body. At 1-5 km depth, the temperature is relatively stable because the heat flow is transferred mainly by thermal convection resulting from the extensive fractures [*Younker et. al*, 1982]. However, the different extent of mineralization caused by brine fluid upwelling and mixing still causes the variation of lithological composition relative to the intrusive body (Figure 30) [*McKibben et al.*, 1987]. From shallow area (further from intrusion) to deep area (closer to intrusion), the lithological composition changes from slightly altered reservoir rocks to extensively hydrothermally altered, highly fractured reservoir, and for the deep area (~3-5 km depth), fracture density is higher [*Younker et. al*, 1982]. The fractures can be created or

reactivated after being filled or sealed by faulting or hydraulic fracturing resulting from high pore pressure perturbation [*Grindley and Browne*, 1976]. The width of a seismic cluster driven by fluid injection in naturally fractured crystalline rock (deeper layer) is wider than that for weak sedimentary rock (upper layer), because the natural fracture network allows for fast fluid transport into neighboring fractures and drives this highly fractured zone [*Zang*, 2014]. Moreover, our results are in agreement with *McGuire et al.* [2015]: induced microseismicity is concentrated in a reduced porosity, hydrothermally altered, dense, highly fractured layer (~3-5 km depth) [*Clayton et al.*, 1968] instead of the unaltered sandstone layer.

Effect of fluid and fault distribution

As discussed in *Lengline et al.* [2014], slip on the interface, no matter earthquake rupture or aseismic slip, can both create new pathways for fluid and change the available space for fluid along interface, which cause locally rapid pore pressure variation. The rapid variation of pore pressure leads to the changes of stress loading rate and effective normal stress. The rapid increase of pore pressure reduces local effective normal stress [*Zoback*, 2008] and induced clusters of events. Fluid migration and diffusion [*Chen and Shearer*, 2011] reduce the pore pressure as well as normal stress, which cause the rapid end of cluster. As a result, where rapid fluid pressure variation is the predominant factor affecting the stress change, there would be a lot of mixtures which does not obey Omori's law and has high aftershock productivity. And the increase of pore pressure also reduced differential stress which leads to reduced stress drop [*Goertz-Allmann et al.*, 2011]. Moreover, frequent fluid injection shortens the

inter-seismic period for strain energy accumulation and induces a large amount of small events, corresponding to the high *b*-value near injection wells.

However, besides fluid stress, there are some other factors also affecting the fault strength. The aseismic creep can change the loading stress and lead to the change of seismic rate and LME frequency [*Mcguire et al.,* 2015]. And in the SSGF, there are some large magnitude events with low *b*-value and high stress drop (Figure 28 b and d) located at shallow area, where there are numerous shallow fault observed in *Hulen et al.* [2003] (Figure 4). And with the increase of depth, the decreased scale of fault and increased fault density lead to smaller scale rupture process. As a result, the highly fractured reservoir zone near injection well has fewer large earthquakes but more small earthquakes, corresponding to relatively higher *b*-value. And because of the high density fracture, the applied shear stress can easily transfer to neighboring fractures, which is hard to nucleate potential energy and cause events with high stress drop. In conclusion, the existence of aftershock sequences and large magnitude events (large circle in Figures 28b, c and d) in the shallow, slightly altered zone indicates the existence of faults with suitable orientation and higher fault strength. For the deeper seismogenic zone (3.5-5km), reduced porosity, fluid injection, and convective flow of pore fluid all increase pore pressure and reduce effective normal stress. This would result in an activation of rupture along major pre-existing fractures, produce new fracture, reactivate a sealed fracture, and induce a large volume of small events with low stress drop repeatedly in the same area [*McGuire et al.*, 2015; *Schoenball et al.*, 2015].

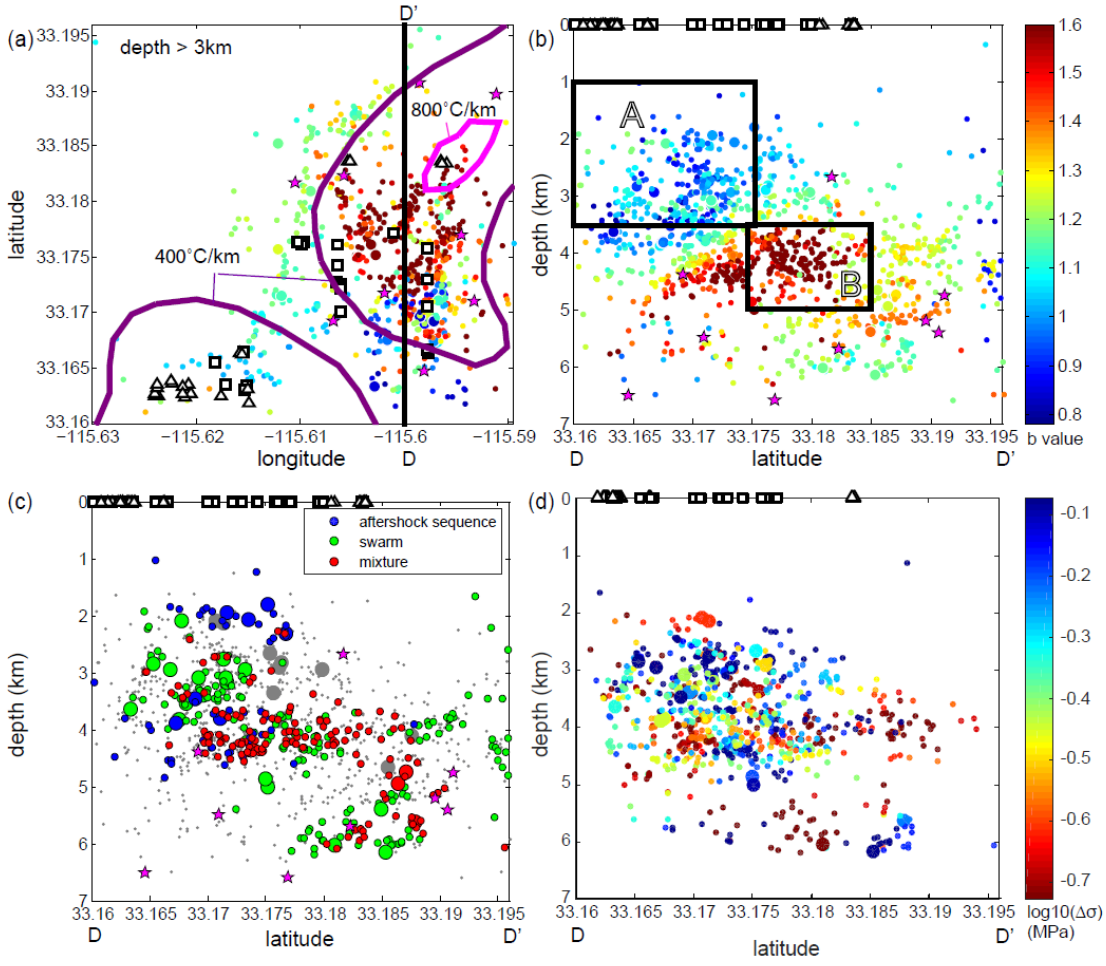

Figure 28. *B*-value, cluster-type, and stress drop distributions within the middle cluster (black box in Figures 12a, 13a and 20a). (a) Map view of *b*-value distributions (for clarity reasons, only events >3 km are plotted), and contour lines of 800°C/km and 400°C/km geothermal gradient. (b) Cross-section view of *b*-value along DD' profile (latitude versus depth). For both (a) and (b), events are colored with *b*-value. (c) Cross-section view of clustering type along DD' profile (latitude versus depth). Events within clusters are colored according to clustering type, non-clustered events are shown in grey dots. (d) Cross-section view of stress drop variation along DD' profile (latitude versus depth). Events are colored by the median stress drops of their nearest 10 events. Injections wells are white squares, and productions wells are white triangles. Historic large magnitude events with $\boldsymbol{M_L \geq 4}$ since 1981 are plotted by magenta star.

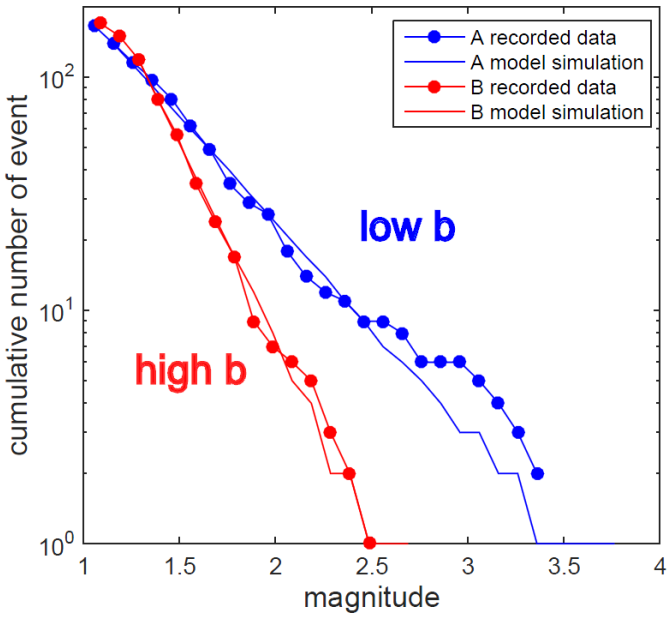

Figure 29. Example magnitude-frequency distribution for events within the two boxes in Figure 28b.

The main differences between mixture-type and aftershock/swarms are the less-favorable Omori's decay, higher aftershock productivity and shorter duration (Figure 10), but is possibly related to the rapid activation of connected fractures. The higher aftershock productivity is consistent with statistical modeling of induced seismicity in Oklahoma and Arkansas [*Llenos and Michael*, 2013], and so it is potentially a common signature of fluid-induced seismicity.

I therefore interpret the mixture-type clustering, higher aftershock productivity, low stress drop and high *b*-value as the characteristics of directly induced seismicity due to interaction of frequent rapid local fluid perturbations, heat flow convection and a highly fractured zone with small-size faults, which limit the maximum magnitude. For regions further from the injection well zones, the dominantly aftershock/swarm-type clustering, lower *b*-value, high stress drop, and more planar fault orientations suggest

that larger pre-existing faults are re-activated by distributed fluid pressure diffusion in a relatively low temperature zone, which is also supported by existence of fluid-driven migration within the broader area [*Chen and Shearer*, 2011].

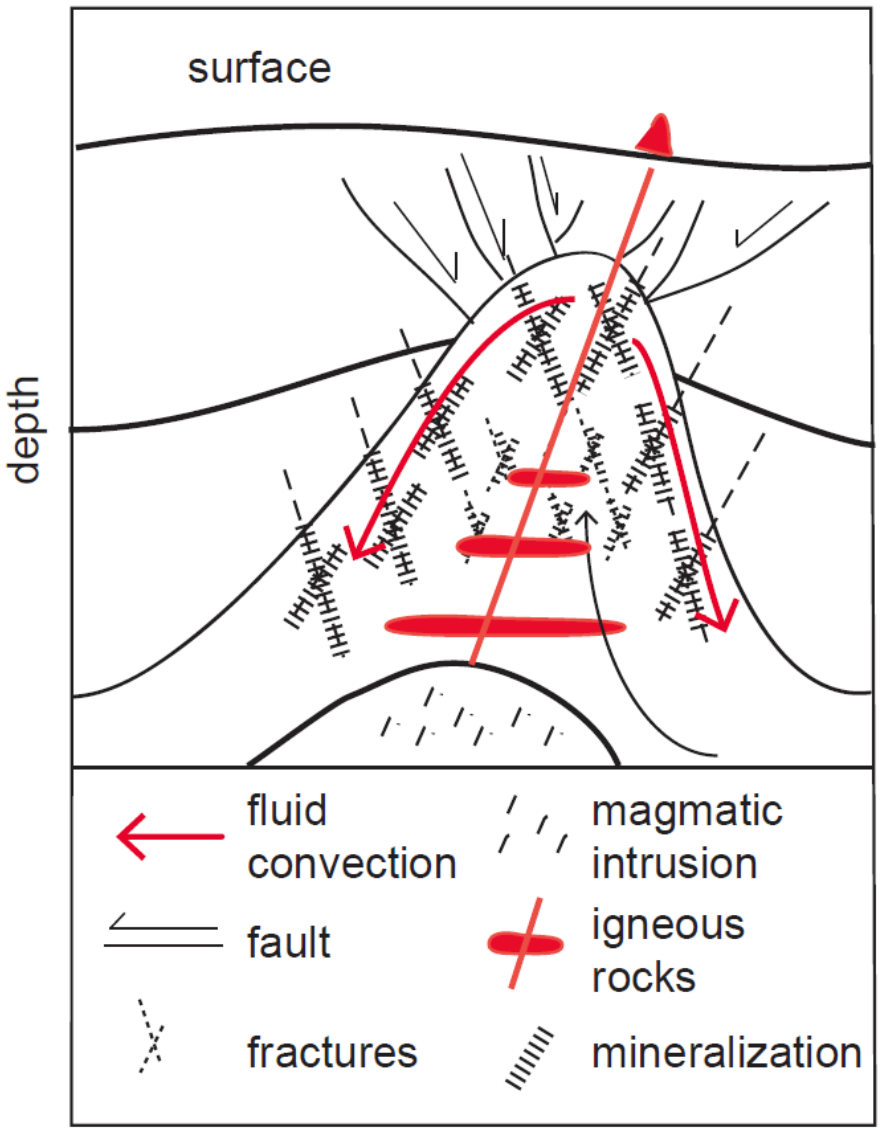

Figure 30. A schematic cartoon for mineralization by brine upwelling and mixing in the SSGF modified from Figure 10 of *Williams and McKibben et al.* [1989] and Figure 12 of *McKibben et al.* [1987]. The faults in the shallow layer are after the major faults interpreted by *Hulen et al.* [2003].

Conclusion

I auto-pick S-wave phase arrivals on triggered waveforms from a local borehole network, relocate 7348 microearthquakes using a 3D velocity model, absolute and differential arrival times based on double-difference algorithm [*Zhang and Thurber*, 2003]. I apply a single-link clustering method based on neighbor distance and inter-event time to our relocated earthquake catalog for the Salton Sea Geothermal Field. The resulting clusters are divided into different types based on magnitude time and moment release history. Detailed investigation of cluster properties suggests that the mixture type tends to occur within close proximity to injection wells and has higher aftershock productivity and lower mainshock magnitude. The magnitude frequency distribution of regions with mixture-type sequences confirms this conclusion. Also, the analysis of the source spectra for 1954 earthquakes in the SSGF with a stack-and-invert EGF method reveals lateral and depth variation of stress drop. The stress drops are much lower than most regions in Southern California. Lower stress drops are observed near injection wells.

For injection well zones, the observed large amount of small magnitude events, higher *b*-value, low stress drop and mixtures in the middle zone of our study region are possibly caused by the interaction among pre-existing extensive fractures and rapid fluid perturbation in high temperature regions. In shallower zone, lower *b*-value, high stress drop, more large magnitude events, as well as high probability of LME suggest distributed fluid diffusion activating larger stronger faults [*Hulen et al.*, 2003].

The spatial variations of geothermal operations, heat transfer mechanism, and rock properties variation caused by intrusion make the strong variation of seismic

characteristic variations within Salton Sea Geothermal Field. And the parameters I used in this study shows obvious spatial correlations with geothermal operation and geological context.

The occurrence of mixture and repeating earthquakes indicates that, instead of regional long-term process, the predominant factor affecting mixture varies rapidly in short timescale. And the most likely candidate is fluid pressure variation caused by geothermal operation.

B-value shows the relationship between event size and frequency. High *b*-value area is more likely to have smaller earthquake compared with larger earthquake. It can be used to assess the likelihood of the occurrence of large magnitude events. And *b*-value anomalies can be related to stress-level, lithology and temperature.

LME probability distribution, which is derived from *b*-value, provides a direct view of relative safer area and more dangerous area. And we can get the probability of event exceeding the magnitude we care to assess the earthquake hazard.

Stress drop is a parameter with physical meaning. It helps us to link the observed seismicity to physical process. The value of stress drop is related to stress state along the fault and the strength of fault, which may be alternated by some environmental conditions like fluid pressure, aseismic slip, and lithology.

And these parameters can be linked to the properties of fault and environmental conditions. It would be helpful to use them as important inputs for assessing earthquake hazards caused by anthropogenic activities, incorporating systemic spatial variations should improve our knowledge of expected earthquake hazards.

References

Abercrombie, R. E., Earthquake source scaling relationships from -1 to 5 M_L using seismograms recorded at 2.5 km depth, *J. Geophys. Res*, 100, 24015–24036, 1995.

Abercrombie, R. E., P. Leary, Source parameters of small earthquakes recorded at 2.5 km depth, Cajon Pass, southern California: Implications for earthquake scaling, *Geophys. Res. Lett.*, 20, 1511–1514, 1993.

Aki, K.(1965), Maximum likelihood estimate of b in the formula log N = a − b M and its confidence limits, *Bull. Earthquake Res. Inst. Univ. Tokyo*, *43*, 237–239.

Allmann, B., and P. Shearer (2007), Spatial and temporal stress drop variations in small earthquakes near Parkfield, California,*J. Geophys. Res.*, 112, B04305, doi:10.1029/2006JB004395.

Amitrano, D. (2003), Brittle-ductile transition and associated seismicity: Experimental and numerical studies and relationship with the b value, *J. Geophys. Res.*, *108*(B1), 1–15, doi:10.1029/2001JB000680.

Bachmann, C. E., S. Wiemer, B. P. Goertz-Allmann, and J. Woessner (2012), Influence of pore-pressure on the event-size distribution of induced earthquakes, *Geophys. Res. Lett.*, *39*(9), 1–7, doi:10.1029/2012GL051480.

Barton, C., Moos, D. and K. Tezuka (2009), Geomechanical wellbore imaging: Implications for reservoir fracture permeability, *AAPG bulletin*, *93*(11), 1551-1569.

Ben-Zion, Y. (2008), Collective behavior of earthquakes and faults: Continuum-discrete transitions, progressive evolutionary changes, and different dynamic regimes, *Rev. Geophys.*, *46*, RG4006, doi:10.1029/2008RG000260.

Brodsky, E. E., and L. J. Lajoie (2013), Anthropogenic seismicity rates and operational parameters at the Salton Sea Geothermal Field., *Science*, *341*(6145), 543–6, doi:10.1126/science.1239213.

Brothers, D. S., N. W. Driscoll, G. M. Kent, A. J. Harding, J. M. Babcock, and R. L. Baskin (2009), Tectonic evolution of the Salton Sea inferred from seismic reflection data, *Nat. Geosci.*, *2*(8), 581–584, doi:10.1038/ngeo590.

Brune, J. N. (1970), Tectonic stress and the spectra of seismic shear waves, *J. Geophys. Res.*, 75, 4997–5009.

Catchings, R. D., M. J. Rymer, M. D. Goldman, R. B. Lohman, and J. J. McGuire (2010), The Obsidian Creep Project: Seismic Imaging in the Brawley Seismic Zone and Salton Sea Geothermal Field, Imperial County, California, Abstract T53B-2122 presented at 2010 Fall Meeting, AGU, San Francisco, Calif., 13–17 Dec.

Chen, X., and P. M. Shearer (2011), Comprehensive analysis of earthquake source spectra and swarms in the Salton Trough, California, *J. Geophys. Res. Solid Earth*, *116*(9), 1–17, doi:10.1029/2011JB008263.

Chen, X., P. M. Shearer, and R. E. Abercrombie (2012), Spatial migration of earthquakes within seismic clusters in Southern California: Evidence for fluid diffusion, J. Geophys. Res., 117, B04301, doi:10.1029/2011JB008973.

Clayton, R. N., L. J. P. Muffler, and D. E. White (1968), Oxygen isotope study of calcite and silicates of the River Ranch No. 1 Well, Salton Sea Geothermal Field, California, *Am. J. Sci*., *266*, 968–979.

Crowell, B. W., Y. Bock, D. T. Sandwell, and Y. Fialko (2013), Geodetic investigation into the deformation of the Salton Trough, *J. Geophys. Res. Solid Earth*, 118, 5030–5039.

Davis, S. D., and C. Frohlich (1991), Single-Link Cluster Analysis, Synthetic Earthquake Catalogues, and Aftershock Identification, *Geophys. J. Int.*, *104*(2), 289–306, doi:10.1111/j.1365-246X.1991.tb02512.x.

Davis, S. D., and C. Frohlich (1993), Did (or will) fluid injection cause earthquakes? Criteria for a rational assessment, *Seismol. Res. Lett.*, *64*, 207–224.

Dieterich, J. (1994). A constitutive law for rate of earthquake production and its application to earthquake clustering. *Journal of Geophysical Research: Solid Earth*, *99*(B2), 2601-2618.

Ellsworth, W. L. (2013), Injection-induced earthquakes. Science, *341*(6142), 1225942.

Eshelby, J. D. (1957), The determination of the elastic field of an ellipsoidal inclusion and related problems, *Proc. Roy. Soc. London, Ser. A*, *241*, 376–396.

Evans, K. F. (2005), Permeability creation and damage due to massive fluid injections into granite at 3.5 km at Soultz: 2. Critical stress and fracture strength, *J. Geophys. Res.*, B04204, doi:10.1029/2004JB003169.

Feng, Q., and J. M. Lees (1998), Microseismicity, stress, and fracture in the Coso geothermal field, California, *Tectonophysics*, *289*(1-3), 221–238, doi:10.1016/S0040-1951(97)00317-X.

Frohlich, C. (1987), Aftershocks and temporal clustering of deep earthquakes, *J. geophys. Res.*, *92*, 13944-13956.

Frohlich, C., D. Scott, G. Sciences, and A. P. O. Box (1990), Single-link cluster analysis as a method to evaluate spatial and temporal properties of earthquake catalogues, *Geophys. J. Int.*, *100*, 19–32.

Frohlich, C., C. Hayward, B. Stump, and E. Potter (2011), The Dallas-Fort Worth earthquake sequence: October 2008 through May 2009, *Bull. Seismol. Soc. Am.*, 101, 327–340.

Giardini, D., S. Wiemer, D. Fah, and N. Deichmann (2004), Seismic hazard assessment of switzerland, 2004, technical report, Swiss Seismol. Serv., ETH Zurich, Zurich, Switzerland.

Goebel, T. H. W., T. Candela, C. G. Sammis, T. W. Becker, G. Dresen, and D. Schorlemmer (2013), Seismic event distributions and off-fault damage during frictional sliding of saw-cut surfaces with pre-defined roughness, *Geophys. J. Int.*, *196*(1), 612–625, doi:10.1093/gji/ggt401.

Goertz-Allmann, B. P., A. Goertz, and S. Wiemer (2011), Stress drop variations of induced earthquakes at the Basel geothermal site, *Geophys. Res. Lett.*, 38, L09308, doi:10.1029/2011GL047498.

Got, J. L., & Fréchet, J. (1993). Origins of amplitude variations in seismic doublets: source or attenuation process?. *Geophysical Journal International,114*(2), 325-340.

Grindley, G.W. and P.R.L. Browne (1976), Structural and hydrological factors controlling the permeabilities of some hot-water geothermal wells. In: Proceedings Second United Nations Symposium on Development and Use of Geothermal Resources, Vol. 1. Lawrence Berkeley Laboratory, Berkeley, Calif., 379--386.

Grünthal, G. (2014), Induced seismicity related to geothermal projects versus natural tectonic earthquakes and other types of induced seismic events in Central Europe, *Geothermics*, *52*, 22–35, doi:10.1016/j.geothermics.2013.09.009.

Guo, Z., and Y. Ogata (1997), Statistical relations between the parameters of aftershocks in time, space, and magnitude. *J. Geophys. Res. Solid Earth*, *102*(B2), 2857-2873.

Gutenberg, B., and C. F. Richter (1942), Earthquake magnitude intensity, energy, and acceleration, *Bull. Seismol. Soc. Am.*, *32*, 163–191.

Hainzl, S. (2003), Self-organization of earthquake swarms, *J. Geodynamics*, 35, 157-172.

Hardebeck, J. L., and E. Hauksson (1997), Static stress drop in the 1994 Northridge, California, aftershock sequence, *Bull. Seismol. Soc. Am.*, 87, 1495–1501.

Hardebeck, J. L., and A. Aron (2009), Earthquake stress drops and inferred fault strength on the Hayward Fault, east San Francisco Bay, California, Bull. Seismol. Soc. Am., 99(3), 1801–1814, doi:10.1785/0120080242.

Hauksson, E., W. Yang, and P. M. Shearer (2012), Waveform Relocated Earthquake Catalog for Southern California (1981 to June 2011), *Bull. Seismol. Soc. Am.*, *102*(5), 2239–2244, doi:10.1785/0120120010.

Hough, S. E., J. M. Lees, and F. Monastero (1999), Attenuation and source properties at the Coso Geothermal area, California,*Bull. Seismol. Soc. Am.*, 89, 1606–1619.

Hough, S. E. and H. Kanamori (2002), Source Properties of Earthquakes near the Salton Sea Triggered by the 16 October 1999 M 7.1 Hector Mine, California, Earthquake, *Bull. Seismol. Soc. Am.*, *92*(4), 1281–1289, doi:10.1785/0120000910.

Hulen, J. B., and F. S. Pulka (2001), Newly-discovered, ancient extrusive rhyolite in the Salton Sea Geothermal Field, Imperial Valley, California, paper presented at Twenty-Sixth Workshop on Geothermal Reservoir Engineering, Stanford Univ., Stanford, Calif.

Hulen, J. B., D. Norton, D. Kaspereit, L. Murray, T. van de Putte, and M. Wright (2003), Geology and a working conceptual model of the Obsidian Butte (Unit 6) sector of the Salton Sea Geothermal Field, California, *Geoth. Resour. Counc. Trans.*, 27, 227–240.

Jones, L. E., and D. V. Helmberger (1996), Seismicity and stress-drop in the eastern Transverse ranges, southern California,*Geophys. Res. Lett.*, 23, 233–236.

Kanamori, H. and Brodsky, E. E. (2004). The physics of earthquakes. *Reports on Progress in Physics*, *67*(8), 1429.

Kisslinger, C. (1996), Aftershocks and fault-zone properties, *Advances in Geophysics*, *38*, 1–36, Academic, San Diego, Calif.

Kwiatek, G., K. Plenkers, M. Nakatani, Y. Yabe, G. Dresen, and JAGUARS-Group (2010), Frequency-magnitude characteristics down to magnitude −4.4 for induced seismicity recorded at Mponeng gold mine, South Africa, *Bull. Seismol. Soc. Am.*, 100(3),1165–1173.

Lengliné, O., and Got, J. L. (2011). Rupture directivity of microearthquake sequences near Parkfield, California. *Geophysical Research Letters*, *38*(8).

Lengliné, O., Lamourette, L., Vivin, L., Cuenot, N., and Schmittbuhl, J. (2014). Fluid‐induced earthquakes with variable stress drop. *Journal of Geophysical Research: Solid Earth*, *119*(12), 8900-8913.

Llenos, A. L., J. J. McGuire, and Y. Ogata (2009), Modeling seismic swarms triggered by aseismic transients, *Earth Planet. Sci. Lett.*, *281*(1-2), 59–69, doi:10.1016/j.epsl.2009.02.011.

Llenos, A. L., and A. J. Michael (2013), Modeling earthquake rate changes in Oklahoma and Arkansas: Possible Signatures of induced seismicity, *Bull. Seismol. Soc. Am.*, *103*(5), 2850–2861, doi:10.1785/0120130017.

Lohman, R. B., and J. J. McGuire (2007), Earthquake swarms driven by aseismic creep in the Salton Trough, California, *J. Geophys. Res. Solid Earth*, *112*(4), 1–10, doi:10.1029/2006JB004596.

Madariaga, R.(1976), Dynamics of an expanding circular fault, *Bull. Seismol. Soc. Amer.*, 66.

McGarr, A. (1976), Seismic moments and volume changes, *J. Geophys. Res.*, **81**, 1487–1494.

McGuire, J. J., R. B. Lohman, R. D. Catchings, M. J. Rymer, and M. R. Goldman (2015), Relationships between seismic velocity, metamorphism, and seismic and aseismic fault slip in the Salton Sea Geothermal Field region, *J. Geophys. Res. Solid Earth*, *120*, doi:10.1002/2014JB011579.

McKibben, M. A., A. E., Williams, W. A., Elders, & C. S., Eldridge (1987). Saline brines and metallogenesis in a modern sediment-filled rift: the Salton Sea geothermal system, California, USA. *Applied geochemistry*, *2*(5-6), 563-578.

Mogi, K. (1963), Some discussions on aftershocks, foreshocks and earthquake swarms: The fracture of a semi-infinite body caused by an inner stress origin and its relation to the earthquake phenomena (third paper), *Bull. Earthquake Res. Inst., Univ. Tokyo*, *41*, 615–658.

Muffler, L. J., and D. E. White (1969), Active metamorphism of upper Cenozoic sediments in the Salton Sea geothermal field and the Salton Trough, southeastern California. *Geological Society of America Bulletin*, *80*(2), 157-182.

Mukuhira, Y., H. Asanuma, H. Niitsuma, M. Häring, and N. Deichmann (2010), Estimation of source parameter of microseismic events with large magnitude collected at Basel, Switzerland in 2006, GRC Trans., 34, 407–412.

Neuville, A., R. Toussaint, and J. Schmittbuhl (2010), Hydrothermal coupling in a self-affine rough fracture, *Phys. Rev. E, 82*(3),36,317,

Nuannin, P. (2006). The potential of *b*-value variations as earthquake precursors for small and large events.

Omori, F. (1894), On the aftershocks of earthquakes, *J. College Sci.*, Imperial Univ. Tokyo, *7*,111–200.

Park, J., C. R. Lindberg, F. L. Vernon (1987), Multitaper spectral analysis of high frequency seismograms, *J. Geophys. Res.*, 92, 12, 675–12,684.

Reyners, M., D. Eberhart-Phillips, and G. Stuart (2007), The role of fluids in lower-crustal earthquakes near continental rifts, *Nature*, *446*, 1075–1078.

Roland, E., and J. J. McGuire (2009), Earthquake swarms on transform faults, *Geophys. J. Int.*, *178*(3), 1677–1690, doi:10.1111/j.1365-246X.2009.04214.x.

Schoenball, M., N. C. Davatzes, and J. M. G. Glen (2015), Differentiating induced and natural seismicity using space-time-magnitude statistics applied to the Coso Geothermal field, *Geophys. Res. Lett.*, *42*(15), 6221-6228, doi:10.1002/2015GL064772.

Scholz, C. H. (1990), The Mechanics of Earthquakes and Faulting, 439, Cambridge University Press, New York.

Scholz, C. H., and J. C. Contreras (1998), Mechanics of continental rift architecture, *Geology*, *26*,967–970.

Schorlemmer, D., S. Wiemer and M. Wyss (2004), Earthquake statistics at parkfield: 1. Stationarity of b values, *Journal of Geophysical Research*, *109*, doi: 10.1029/2004JB003234.

Schorlemmer, D., and S. Wiemer (2005), Microseismicity data forecast rupture area, *Nature*, *434*, 1086, doi:10.1038/4341086a.

Sellers, E. J., M. O. Kataka, and L. M. Linzer (2003), Source parameters of acoustic emission events and scaling with mining-induced seismicity, *J. Geophys. Res.*, 108(B9), 2418, doi:10.1029/2001JB000670.

Shapiro, S. A., C. Dinske, and J. Kummerow (2007), Probability of a given-magnitude earthquake induced by a fluid injection, *Geophys. Res. Lett.*, **34**, L22314, doi:10.1029/2007GL031615.

Shapiro, S. A., C. Dinske, C. Langenbruch, and F. Wenzel (2010), Seismogenic index and magnitude probability of earthquakes induced during reservoir fluid stimulations, *Leading Edge*, **29**, 304–309, doi:10.1190/1.3353727.

Shearer, P. M., G. Prieto, and E. Hauksson (2006), Comprehensive analysis of earthquake source spectra in southern California,*J. Geophys. Res.*, doi:10.1029/2005JB003979, in press.

Soosalu, H., J. Key, R. S. White, C. Knox, P. Einarsson, and S. S. Jakobsdóttir (2010), Lower-crustal earthquakes caused by magma movement beneath Askja volcano on the north Iceland rift, *Bull. Volcanol.*, *72*, 55–62, doi:10.1007/s00445-009-0297-3.

Tomic, J., R. E. Abercrombie, and A. F. do Nascimento (2009), Source parameters and rupture velocity of small $M \leq 2.1$ reservoir induced earthquakes, *Geophys. J. Int.*, 179, 1013–1023.

Trifu, C.I. (2002), The mechanism of induced seismicity, *Pure and Applied Geophysics*, *159*(1–3), 617.

Trugman, D. T., P. M. Shearer, A. A. Borsa, and Y. (2016), A comparison of long-term changes in seismicity at the Geysers, Salton Sea, and Coso geothermal fields, *Journal of Geophysical Research: Solid Earth*, *121*, doi:10.1002/2015JB012510.

Utsu, T. (1965), A method for determining the value of b in a formula log n = a-bM showing the magnitude frequency for earthquakes, *Geophys. Bull. Hokkaido Univ.*, *13*, 99–103.

Utsu, T. (1999), Representation and analysis of the earthquake size distribution: A historical review and some new approaches, *Pure Appl. Geophys.*, *155*(2–4), 509–535, doi:10.1007/s000240050276.

Utsu, T., Y. Ogata, and R. S. Matsu'ura (1995), The centenary of the Omori formula for a decay law of aftershock activity, *J. Phys. Earth*, *43*,1–33.

Venkataraman, A., and H. Kanamori (2004), Observational constraints on the fracture energy of subduction zone earthquakes,*J. Geophys. Res.*, 109, B05302, doi:10.1029/2003JB002549.

Vidale, J. E., and P. M. Shearer (2006), A survey of 71 earthquake bursts across southern California: Exploring the role of pore fluid pressure fluctuations and aseismic slip as drivers, *J. Geophys. Res.*, *111*, B05312.

Wiemer, S. (2001), A software package to analyze seismicity: ZMAP, *Seismol. Res. Lett.*, *72*(3), 373–382, doi:10.1785/gssrl.72.3.373.

Wiemer, S., and M. Wyss (1997), Mapping the frequency-magnitude distri- bution in asperities: An improved technique to calculate recurrence times?, J. Geophys. Res., 102, 15,115–15,128.

Wiemer, S. and M. Wyss (2000), Minimum magnitude of completeness in earthquake catalogs: examples from Alaska, the western United States and Japan, *Bull. seism. Soc. Am.*, *90*(4), 859–869.

Williams, A. E., and M. A. McKibben (1989), A brine interface in the Salton Sea geothermal system, California: Fluid geochemical and isotopic characteristics, *Geochim. Cosmochim. Acta*, 53, 1905–1920, doi:10.1016/0016-7037(89)90312-8.

Woessner, J., and S. Wiemer (2005), Assessing the quality of earthquake catalogues: Estimating the magnitude of completeness and its uncertainty, *Bull. Seismol. Soc. Am.*, *95*(2), 684–698, doi:10.1785/0120040007.

Younker, L., P. Kasameyer, and J. Tewhey (1982), Geological, geophysical, and thermal characteristics of the Salton Sea Geothermal Field, California, *Volcanol. Geotherm.*, *12*, 221–258.

Zaliapin, I., A. Gabrielov, V. Keilis-Borok, and H. Wong (2008), Clustering analysis of seismicity and aftershock identification, *Phys. Rev. Lett.*, *101*(1), 4–7, doi:10.1103/PhysRevLett.101.018501.

Zaliapin, I. and Y. Ben-Zion (2011), Asymmetric distribution of aftershocks on large faults in California, *Geophys. J. Int.*, *185*(3), 1288-1304.

Zaliapin, I. and Y. Ben-Zion (2013), Earthquake clusters in southern California I: Identification and stability, *J. Geophys. Res.: Solid Earth*, *118*(6), 2847-2864.

Zaliapin, I. and Y. Ben-Zion (2016), Discriminating characteristics of tectonic and human-induced seismicity, *Bull. Seismol. Soc. Am.*, *106*, doi: 10.1785/0120150211.

Zang, A., V. Oye, P. Jousset, N. Deichmann, R. Gritto, A. McGarr, E. Majer, and D. Bruhn (2014), Analysis of induced seismicity in geothermal reservoirs - An overview, *Geothermics*, *52*, 6–21, doi:10.1016/j.geothermics.2014.06.005.

Zhang, H., and C. H. Thurber (2003), Double-difference tomography: The method and its application to the Hayward fault, California, *Bull. Seismol. Soc. Am.*, *93*, 1875–1889, doi:10.1785/0120020190.

Zhang, Q., and P. M. Shearer (2016), A new method to identify earthquake swarms applied to seismicity near the San Jacinto Fault, California, *Geoophys. J. Int. 205, 995-1005*, doi:10.1093/gji/ggw073.

Zoback, M. D. (2008), Reservoir Geomechanics, Cambridge Univ. Press, New York.

Appendix A: List of frequently used symbols

A	rupture area
a	intercept of the earthquake magnitude-frequency relationship
b	slope of the earthquake magnitude-frequency relationship
β	S-wave velocity
D	seismic slip
d_{ij}	displacement spectra of event i recorded by station j in log domain
EGF	Empirical Green's Function
e_i	source spectra term of event i in log domain
f_c	corner frequency of source spectra obtained using Brune model
$G(f)$	spectra ratio
η_{ij}	spatio-temporal neighboring distance between event i and j
η_{thres}	empirical threshold used in clustering
k	constant that links the rupture dimension to corner frequency
LME	Large Magnitude Event (M≥3 in this study)
M_L	local earthquake magnitude
$\bar{M}$	mean magnitude of chosen events for b-value estimation
M_c	magnitude of completeness
M_{main}	magnitude of the maximum magnitude event in the cluster (s)
M_0	absolute seismic moment
M_w	earthquake magnitude (moment magnitude)
$m_0(i)$	normalized individual moment of event i in its belonging cluster
ΔM	magnitude binning width of the catalogue

N_c	normalized number of clusters (normalized by total number of clusters)
μ	shear modulus
μ_3	third central moment of the cluster
p	probability of an event exceeding a certain magnitude
res_{ij}	residual of the displacement spectra of event i recorded by station j log domain
dr_{ij}	distance between event i and j (km)
dR_j	distance between event j and its nearest neighbor
SSGF	Salton Sea Geothermal Field
s_j	station j's spectra term in log domain
$skew$	the skew of moment release of the cluster
T_d	duration of cluster (hour)
t_{first}	time of the first event in the cluster (s)
t_{max}	normalized timing of the largest event in the cluster
t_{maxmag}	time of the maximum magnitude event in the cluster (s)
t_{median}	median time of the events in the cluster (s)
t^*	centroid time of moment release of the cluster (s)
$t_{k(i,j)}$	travel-time spectra term with travel time k (s), which is the P-wave travel time from event i location to station j location.
dt_{ij}	time difference between event i and j (day)
dT_j	time difference between event j and its nearest neighbor (day)
σ	standard deviation of the third central moment of the cluster
$\Delta\sigma$	stress drop, difference between the stress on the fault plane before and

	after an earthquake
Ω_0	measured relative seismic moment
$X(f), Y(f)$	Fourier spectrum of event x and y estimated using normalized amplitude displacement waveform